Mars Exploration Rover Athena Panoramic Camera (Pancam) investigation

J. F. Bell III,[1] S. W. Squyres,[1] K. E. Herkenhoff,[2] J. N. Maki,[3] H. M. Arneson,[1] D. Brown,[3] S. A. Collins,[3] A. Dingizian,[3] S. T. Elliot,[3] E. C. Hagerott,[3] A. G. Hayes,[1] M. J. Johnson,[1] J. R. Johnson,[2] J. Joseph,[1] K. Kinch,[4,5] M. T. Lemmon,[6] R. V. Morris,[7] L. Scherr,[3] M. Schwochert,[3] M. K. Shepard,[8] G. H. Smith,[9] J. N. Sohl-Dickstein,[1] R. J. Sullivan,[1] W. T. Sullivan,[10] and M. Wadsworth[3]

Received 25 February 2003; revised 20 June 2003; accepted 25 July 2003; published 29 November 2003.

[1] The Panoramic Camera (Pancam) investigation is part of the Athena science payload launched to Mars in 2003 on NASA's twin Mars Exploration Rover (MER) missions. The scientific goals of the Pancam investigation are to assess the high-resolution morphology, topography, and geologic context of each MER landing site, to obtain color images to constrain the mineralogic, photometric, and physical properties of surface materials, and to determine dust and aerosol opacity and physical properties from direct imaging of the Sun and sky. Pancam also provides mission support measurements for the rovers, including Sun-finding for rover navigation, hazard identification and digital terrain modeling to help guide long-term rover traverse decisions, high-resolution imaging to help guide the selection of in situ sampling targets, and acquisition of education and public outreach products. The Pancam optical, mechanical, and electronics design were optimized to achieve these science and mission support goals. Pancam is a multispectral, stereoscopic, panoramic imaging system consisting of two digital cameras mounted on a mast 1.5 m above the Martian surface. The mast allows Pancam to image the full 360° in azimuth and ±90° in elevation. Each Pancam camera utilizes a 1024 × 1024 active imaging area frame transfer CCD detector array. The Pancam optics have an effective focal length of 43 mm and a focal ratio of *f*/20, yielding an instantaneous field of view of 0.27 mrad/pixel and a field of view of 16° × 16°. Each rover's two Pancam "eyes" are separated by 30 cm and have a 1° toe-in to provide adequate stereo parallax. Each eye also includes a small eight position filter wheel to allow surface mineralogic studies, multispectral sky imaging, and direct Sun imaging in the 400–1100 nm wavelength region. Pancam was designed and calibrated to operate within specifications on Mars at temperatures from −55° to +5°C. An onboard calibration target and fiducial marks provide the capability to validate the radiometric and geometric calibration on Mars. *INDEX TERMS:* 6225 Planetology: Solar System Objects: Mars; *KEYWORDS:* Mars, multispectral imaging, space missions, Mars Exploration Rover

Citation: Bell, J. F., III, et al., Mars Exploration Rover Athena Panoramic Camera (Pancam) investigation, *J. Geophys. Res.*, *108*(E12), 8063, doi:10.1029/2003JE002070, 2003.

[1]Department of Astronomy, Cornell University, Ithaca, New York, USA.
[2]U.S. Geological Survey, Flagstaff, Arizona, USA.
[3]Jet Propulsion Laboratory, California Institute of Technology, Pasadena, California, USA.
[4]Neils Bohr Institute, University of Copenhagen, Copenhagen, Denmark.
[5]Now at Institute for Physics and Astronomy, University of Aarhus, Aarhus, Denmark.
[6]Department of Atmospheric Science, Texas A&M University, College Station, Texas, USA.
[7]NASA Johnson Space Center, Houston, Texas, USA.
[8]Department of Geography and Geosciences, Bloomsburg University, Bloomsburg, Pennsylvania, USA.
[9]GHS Optics, Pasadena, California, USA.
[10]Department of Astronomy, University of Washington, Seattle, Washington, USA.

0148-0227/03/2003JE002070$09.00

1. Introduction

[2] The history of Mars exploration extends from systematic telescopic observations begun more than a century ago to the current era of spacecraft orbiters and landers/rovers. The first successful Mars surface missions were the Viking Landers, which returned spectacular images, meteorologic data, and in situ compositional information over the course of more than two Mars years each (VL1: 1976–1982; VL2: 1976–1980). The Viking Lander imaging investigations provided the first close-up assessment of the detailed geomorphology, color, and photometric properties of surface soils and rocks as well as atmospheric aerosols [*Huck et al.*, 1975; *Patterson et al.*, 1977]. Though the two Viking landing sites were chosen primarily for

engineering safety considerations rather than science potential, both missions ultimately provided a substantial wealth of new information about the surface of Mars, including more than 1400 images of the two landing sites [e.g., *Mutch et al.*, 1976; *Pollack et al.*, 1979; *Carr*, 1981; *Sharp and Malin*, 1984; *Arvidson et al.*, 1989].

[3] More than 15 years later, the Mars Pathfinder mission provided the next opportunity for landed imaging and other in situ investigations, including the first rover operations on Mars [*Rover Team*, 1997]. The Imager for Mars Pathfinder (IMP) investigation [*Smith et al.*, 1997a] was a substantial technologic advance over the Viking Lander cameras, and collected more than 16,000 multispectral CCD images of a landing site specifically selected for its potential to reveal information on the past history of water on Mars [e.g., *Golombek*, 1997]. Like Viking, Pathfinder acquired exciting and unique new information on the nature of the Martian surface via a combination of lander and rover imaging and other in situ elemental and meteorological measurements [e.g., *Smith et al.*, 1997b; *Golombek et al.*, 1999].

[4] The next mission to the surface of Mars is the Mars Exploration Rover (MER) mission, which will land two identical rovers at separate landing sites on Mars in early 2004. Each of these rovers (Figure 1) carries an impressive array of science and engineering instruments, and is designed to traverse up to 100 m/sol to make remote sensing and in situ measurements. A subset of rover instruments consisting of three cameras, three spectrometers, an array of magnets, and a rock drilling device constitute the Athena payload, a synergistic collection of science investigations designed to address the goals of the MER mission, which involve investigating the role of water in the geological history of two separate landing sites on Mars [*Squyres et al.*, 2003]. Two of these cameras on each rover form a panoramic, multispectral, stereoscopic camera system called Pancam, which is a key component of the Athena payload. As described in detail in this paper, Pancam represents an important advance in the progression of Mars surface imaging investigations, as it possesses excellent multispectral and dynamic range capabilities similar to those of the IMP camera, and roughly 3 times better spatial resolution compared with cameras on Pathfinder or the Viking Landers. In addition to directly addressing the science goals of the MER mission, the Pancam investigation is also expected to provide essential science support for the other instruments of the Athena payload, as well as operational and navigational support for the rovers themselves.

[5] This paper provides an overview and details of the Pancam investigation. It is divided into four main parts. Section 2 describes the overall scientific objectives of the Pancam investigation and how they help meet the overall objectives of the MER mission as a whole. This section also discusses how these objectives logically lead to a set of design and measurement requirements for the Pancam instrument. In section 3 we describe the specific details of the instrument itself, including detectors and electronics, optics, filters, calibration target, physical and operational parameters like mass and power, and instrument integration with the Pancam mast assembly (PMA) for articulation. Section 4 describes the current knowledge about preflight Pancam instrument performance, including prelaunch values for many basic calibration coefficients required for data reduction and analysis. Section 5 summarizes expected Pancam operational support roles on Mars and outlines rover commanding, sequencing, and onboard image processing capabilities that will be utilized for Pancam and other MER cameras.

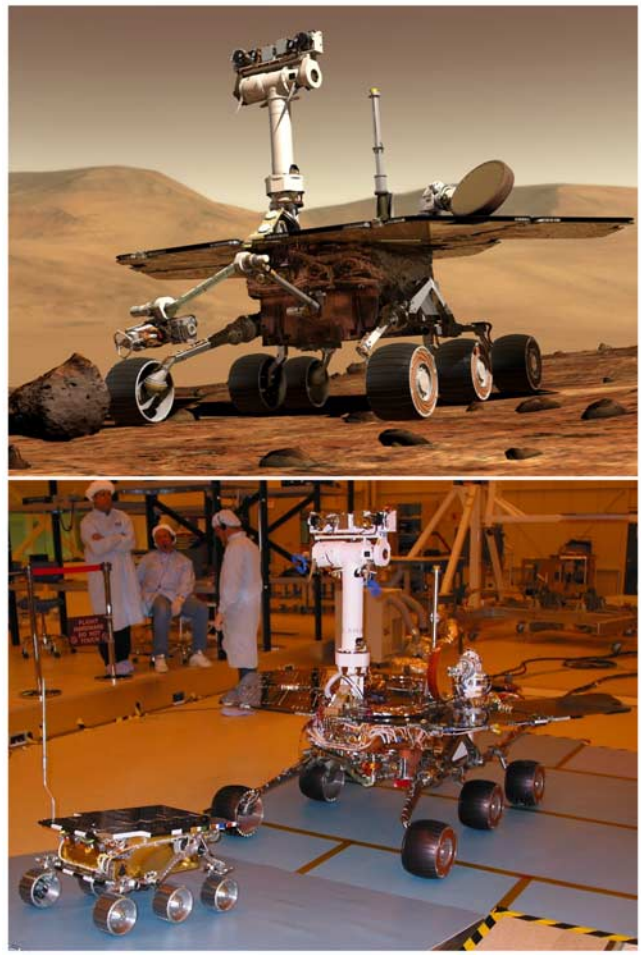

Figure 1. (top) Computer-generated model (courtesy D. Maas, Maas Digital LLC) of the Mars Exploration Rover on Mars. (bottom) Flight model 2 rover (background) in driving configuration, compared to the Pathfinder flight spare rover Marie Curie (foreground). The Pancams are the two outer cameras on the top of the mast assembly.

[6] This paper is intended to provide a broad overview of the Pancam investigation. There is substantial synergy, and some direct overlap, between many of the Pancam topics covered here and similar or related topics for the MER Microscopic Imager [*Herkenhoff et al.*, 2003], Navcam, Hazcam, and DIMES engineering cameras [*Maki et al.*, 2003], and the PMA [*Squyres et al.*, 2003]. This collection of papers is therefore an important initial resource for researchers interested in gaining a full understanding of the broad scope and capabilities of all of the imaging capabilities on the Mars Exploration Rovers.

2. Pancam Investigation Objectives

[7] The primary science goal of the MER Athena investigation is to determine the aqueous, climatic, and geologic

Table 1. Pancam Investigation Objectives

No.	Objective
	Science
1	Obtain monoscopic and stereoscopic image mosaics to assess the morphology, topography, and geologic context of each MER landing site.
2	Obtain multispectral visible to short-wave near-IR images of selected regions to determine surface color and mineralogic properties.
3	Obtain multispectral images over a range of viewing geometries to constrain surface photometric and physical properties.
4	Obtain images of the Sun and Martian sky to constrain aerosol physical and radiative properties.
5	Obtain monoscopic and stereoscopic image mosaics to assess the morphology, topography, and geologic context of each MER landing site.
	Mission Support
1	Serve as the primary Sun-finding camera for rover navigation.
2	Resolve objects on the scale of the rover wheels to distances of ~100 m to help guide navigation decisions.
3	Provide stereo coverage adequate for the generation of digital terrain models to help guide and refine rover traverse decisions.
4	Provide high-resolution images and other context information to guide the selection of the most interesting in situ sampling targets.
5	Support acquisition and release of Education and Public Outreach (E/PO) products.

history of sites on Mars where conditions may have been favorable to the preservation of evidence of prebiotic or biotic processes [*Squyres et al.*, 2003]. Pancam has been designed and will be operated on Mars with the aim of supporting this primary goal and a number of related scientific and measurement objectives.

2.1. Scientific Objectives

[8] The scientific objectives of the Pancam investigation are listed in Table 1. They fall into four specific categories.

2.1.1. Geology/Geomorphology

[9] Substantial information useful for the interpretation of the past history of a landing site can come from simply acquiring images of the surroundings. The MER mission rovers are highly capable in this regard because each is endowed with nine cameras (four stereo pairs and one microimager) plus a descent imaging system on the lander itself. Pancam is the highest spatial resolution stereo imaging system on the rovers. Like the Viking and Pathfinder imaging systems, Pancam has the capability to generate panoramas of the surrounding terrain spanning the full 360° of azimuth. However, the high-resolution capabilities of Pancam (0.27 mrad/pixel instantanous field of view (IFOV), corresponding to ~1 mm/pixel at a range of 3 m from the rover) provide approximately a factor of three better resolving power than the Viking Lander cameras or Mars Pathfinder IMP imaging system.

[10] Pancam's higher spatial resolution enhances the ability to resolve fine-scale structure in rock, soil, and sky images, for example potentially providing finer-scale information on layering, sorting, induration, fracturing, aeolian modification, dust coating, or other rock and soil attributes useful for constraining the origin of surface units [e.g., *Christensen and Moore*, 1992; *Moore et al.*, 1999]. Pancam's high-resolution capabilities also provide the ability to resolve geologic features farther from the cameras than previous missions, providing enhanced information on the local geologic setting and context, rock distribution, topographic trends, etc.

2.1.2. Color/Composition

[11] Pancam is the only MER imaging system with multispectral capabilities. Multispectral panoramic imaging provides information on the mineralogical composition of surface materials that supplements and complements data obtained by other MER instruments. Spectra of Mars in the 400–1100 nm range are sensitive to secondary iron oxide and oxyhydroxide minerals with varying degrees of crystallinity [e.g., *Singer*, 1982; *Sherman et al.*, 1982; *Morris et al.*, 1985, 1993, 2000; *Bell et al.*, 1990], to iron-bearing primary basaltic minerals like pyroxene and olivine [e.g., *Adams*, 1974; *Cloutis et al.*, 1986; *Morris et al.*, 2000], and to additional "exotic" iron-bearing phases such as ferric sulfates, ferric carbonates, or iron-bearing clays [e.g., *Sherman et al.*, 1982; *Cornell and Schwertmann*, 1996]. Multispectral imaging at well-selected wavelengths in the visible to short-wave near-infrared can thus provide insights on the inventory of primary volcanic minerals as well as their secondary weathering products.

[12] Our multispectral imaging data set will also help to determine if there are dust coatings and/or weathering rinds on rocks, and if so, how they compare compositionally to the regolith and, by inference, how weathering processes may have changed with time [e.g., *McSween et al.*, 1999; *Bell et al.*, 2000]. Studies of terrestrial weathered soils and thermodynamic calculations of Mars chemical weathering reactions have demonstrated that the presence or absence of certain types of iron-bearing minerals can be used to constrain surface weathering pathways [e.g., *Gooding*, 1978; *Burns*, 1993; *Bishop et al.*, 1998; *Morris et al.*, 2000]. Pancam's multispectral capabilities focus on detecting and quantifying the abundances of these types of minerals, and this aspect of the investigation provides unique capabilities that, in concert with the other remote sensing and in situ experiments on MER and other previous and current Mars mission experiments, has the potential to provide fundamental new information on Martian climatic variability.

[13] In addition to the general characterization of targets of interest, Pancam's multispectral capabilities can also provide unique and diagnostic information that can be used to find and select potential targets for more detailed in situ investigations with the instruments on the rover's arm. For example, 670/440 nm red/blue ratio images were often used during the Mars Pathfinder mission as a simple proxy for "dustiness" of rocks that could potentially be studied by the Sojourner APXS instrument [*McSween et al.*, 1999; *Bell et al.*, 2000]. Later, more detailed analyses were required to tease out often subtle spectral details among the rocks and soils at the Pathfinder site [e.g., *Bell et al.*, 2002] (S. M. Murchie et al., New insights into the geology of the Mars Pathfinder landing site from spectral and morphologic analysis of the IMP 12-color Super Panorama, submitted to *Icarus*, 2003).

[14] On MER, power and downlink data volume constraints will likely prevent us from acquiring Pancam images of the entire scene around the rover through all of the geology filters. Nominal Pancam multispectral images will include stereo imaging through the 750 nm filters (R2, L2), as well as imaging through the green and blue filters (L5: 535 nm and L6: 483 nm) for "true color" imaging. However, we plan to leverage off the Pathfinder experience to determine the minimum number of Pancam filters needed to adequately assess the spectral variability of the landing site, thus allowing the most interesting targets for potential rover in situ work to be identified rapidly. For example, when time, power, and other resource constraints allow, we might augment nominal Pancam color imaging with additional filters in the near-IR to assess the presence and nature of the 1-μm ferrous absorption band in rocks. Also, we may frequently trade spatial for spectral coverage and obtain "multispectral spot" observations of small, well-chosen targets within just a single Pancam frame (or less), but through all 14 geology filters. The exact implementation of this scheme will depend critically on many factors, including the state of rover health after landing, the rate and fidelity of the high-gain and UHF downlinks established to Earth, and of course the intrinsic spectral variability of the specific landing sites themselves.

2.1.3. Photometry

[15] Studies of the reflectance properties of rocks and soils at well-chosen incidence and emission angles can yield information on their physical properties. When combined with modeling studies, such photometric observations can constrain surface grain size, degree of compaction, macroscopic roughness, and particle internal structure [e.g., *Hapke*, 1981, 1986; *Shepard and Arvidson*, 1999]. Such information is useful for better understanding surface composition derived using remotely sensed data acquired from rover and orbital platforms, and as input to atmospheric scattering models that require surface property information [e.g., *Tomasko et al.*, 1999]. Photometric measurements were obtained of a variety of soil and rock units by the Viking and Mars Pathfinder landers. For example, *Guinness et al.* [1987, 1997] used Viking measurements to infer the presence and properties of both duricrusted and varnished surfaces at the landing sites, and *Johnson et al.* [1999] provided some constraints on the physical properties of soil deposits and rock coatings at the Pathfinder site from dedicated photometric imaging sequences. Pancam and IMP have similar capabilities for targeting images of rocks and soils under a variety of illumination and observing geometries (e.g., at solar opposition points or along a preferred photometric great circle). We will utilize this capability in combination with the other Athena remote sensing and in situ instruments to test and expand upon the surface physical properties models and hypotheses proposed based on Viking and Pathfinder imaging data, in particular those involving the effects of dust and rock coatings.

2.1.4. Sun/Sky Imaging

[16] Pancam serves a dual role on MER as both a multispectral science imager and the primary "Sun camera" for each rover. Details of Pancam's Sun finding role, as well as procedures and algorithms describing its use in navigation functions, are described by *Eisenman et al.* [2002] and *Maki et al.* [2003]. Solar images for scientific purposes will be acquired to monitor dust and cloud opacity. Pancam solar images will be used to develop an in situ calibration based on Beers's law, following a procedure similar to that used on Pathfinder data [*Smith and Lemmon*, 1999]. Both solar filters (L8: 440 nm and R8: 880 nm) are sensitive to dust and large ice particles, while the blue solar filter is also sensitive to small ice particles. Opacity determinations may also be used to provide ground truth estimations based on simultaneous MGS and/or Odyssey orbiter data at several times during the mission.

[17] Sky images are taken for several purposes. Images in horizontal arcs from the low Sun around the sky [cf. *Pollack et al.*, 1995; *Tomasko et al.*, 1999] and vertical arcs from the noon Sun [cf. *Markiewicz et al.*, 1999] constrain dust properties, such as single scattering albedo and single particle scattering phase function. Opacity and sky observations taken close in time to Mini-TES sequences provide constraints on the dust size distribution over a wide range of wavelengths. A monitoring program will also search for changes in dust properties in the event of significant increases or decreases in opacity variations. Dust models lead to the generation of models of diffuse sky illumination onto the surface. Such models can be used to investigate the rate of dust deposition onto lander targets [e.g., *Graff et al.*, 2002; *Johnson et al.*, 2003], and they allow a determination of the spectral effects of diffuse illumination on rock and soil materials that are tilted at incidence angles different from that of the Pancam calibration target. Additionally, images of the horizon can be surveyed for dust devils (although most such search images will likely be taken using the wide-field Navcam cameras [*Maki et al.*, 2003]). Simultaneous observations with orbiting platforms will be pursued to best constrain the size and dust loading of detected dust devils. And finally, cloud surveys can be conducted using Pancam's color capabilities to attempt to distinguish between dust and water ice aerosols as the origin of the clouds. Detection of clouds or dust devils could provide new information on wind circulation patterns at the MER landing sites.

2.2. Design Considerations

[18] The major Pancam science and mission support objectives described above and in Table 1 provide constraints on a set of design and measurement requirements that must be met by the instrument and by the rover and mission systems that support the instrument investigation. The most relevant of these requirements are listed in Table 2. For example, to provide stereo ranging and redundant high-resolution imaging capabilities, and also to double the number of available color filter positions for multispectral imaging, each MER rover carries two Pancam cameras atop the PMA. Pancam must serve many different scientific purposes, requiring imaging of the full scene around the rover, targets on the rover itself, and the full Martian sky. We therefore selected a mechanical design that allows pointing of both cameras over 360° in azimuth, and 180° in elevation. To provide the best possible views of distant terrain, the cameras were placed as high above the ground as feasible without requiring the PMA to have more than one mast deployment actuator. Camera placement was also chosen to provide a straightforward translation with the boresight of the Mini-TES in order to maximize the ease with which Pancam and Mini-TES data can be coregistered.

Table 2. MER Requirements Relevant to Pancam Calibration and Testing

Level	Requirement
1	Acquire at least one RGB and at least one stereo 360° panoramic image of each landing site with the Pancam. Image one exposed rock that is also analyzed by another instrument.
1	Drive the rovers to a total of at least eight separate locations and use the instrument suite to investigate context and diversity of the environment.
2	The Project System shall ensure that the quality of the calibration of the science instruments be sufficient to satisfy the requirements and objectives in the Science Requirements Document and the Level 1 science requirements.
2	It shall be possible to produce radiometrically calibrated images from the Pancam and Mini-TES observations on Mars, using measurements of calibration targets on Mars.
3	The Mission System shall have the capability to coregister the Mini-TES, Pancam, and Navcam data to an accuracy of 0.27 mrad (one Pancam pixel).
3	The rover shall have at least four fiducial marks that are visible to the Pancam and whose positions can be known to within 1.5 mm (0.2 mm desired) with respect to the Pancam mast base and which are spaced over a wide range of azimuth and elevation.
3	The Pancam calibration target placement shall minimize the amount of diffuse or reflected sunlight from rover structures that could provide ''contamination'' illumination of the target.
3	The horizontal boresight separation of the Pancam cameras shall be between 20 and 30 cm (±0.5 cm).
3	The Flight System shall ensure that Pancam shall be able to provide Sun knowledge.
3	The PMA shall provide Pancam azimuthal pointing placement to an accuracy of ±2° relative to the actuator hardstop.
3	The PMA shall provide Pancam elevation pointing placement to an accuracy of ±2° relative to the actuator hardstop.
3	The PMA shall provide Pancam azimuthal pointing knowledge to an accuracy of ±0.1° relative to the actuator hardstop.
3	The PMA shall provide Pancam elevation pointing knowledge to an accuracy of ±0.1° relative to the actuator hardstop.
3	The Pancam stereo pair shall have a toe-in of 1° ± 0.25° half angle.
3	The Pancam stereo pair CCDs shall have a rotational coalignment (twist) about boresight relative to each other of ±0.1°.
3	The Pancam stereo pair shall have a relative elevation alignment of <28 mrad (1.60°).
3	The Pancam instantaneous field of view shall be 0.28 ± 0.02 mrad/pixel on axis.
3	The Pancam shall be capable of imaging over the spectral range of 400–1100 nm.
3	The Pancam shall have an effective depth of field of 1.5 m to infinity.
3	The Pancam shall have an MTF of ≥0.30 @ 30 lp/mm over spectral band pass (polychromatic).
3	The Pancam optical design shall minimize the contributions of stray and scattered light onto the CCD.
3	The radiometric calibration of the Pancam shall be performed with an absolute accuracy of ≤7%.
3	The radiometric calibration of the Pancam shall be performed with a relative (pixel-to-pixel) accuracy of ≤1%.
3	The Pancam signal to noise ratio shall be ≥200 for exposures of 50% full well over all spectral band passes and within the operating temperature range.
3	Each Pancam shall have a temperature sensor, accurate to ±2°C, on the CCD package that can be read out and associated with the image data in telemetry.
3	The Pancam shall be able to have the Sun in its field of view (powered and unpowered) and not sustain permanent damage.
4	The Pancam working *f*/# shall be *f*/20 ± 1.
4	The Pancam operating temperature within calibrated specifications is −55 ± 2°C to +5 ± 2°C.

[19] One of the most important design choices for Pancam was its angular resolution. The selected requirement of 0.28 ± 0.02 mrad/pixel satisfies two needs. First, it provides the equivalent of 20/20 human vision. The rovers function as robotic field geologists, controlled remotely by human operators. We know that 20/20 vision in the field, when coupled with surface mobility, provides a good capability for a human geologist to make observations and to formulate and test hypotheses based on these observations. Second, a resolution of 0.28 ± 0.02 mrad/pixel is an appropriate value for assessment of distant rover obstacles. This value would provide a spatial resolution of 2.8 cm/pixel at a range of 100 m, which is the maximum distance that the MER rovers can be expected to traverse in one sol. The rovers can be obstructed by terrain obstacles larger than 20–25 cm, and experience from prototype rovers and the Pathfinder Sojourner rover shows that geologic obstacles must be at least 5–8 pixels across (~14–22 cm at 100 m) in order to be assessed adequately. Resolution of 0.28 ± 0.02 mrad/pixel therefore provides the necessary obstacle recognition capability out to the maximum range that the rover might travel in a sol.

[20] Other camera characteristics were established once the angular resolution was chosen. Because of the desirability of having a single electrical interface for all rover cameras, Pancam was designed with the same CCD and electronics as the Microscopic Imager, Navcams, and Hazcams. The image format of 1024 × 1024 pixels fixed the field of view of Pancam at 16° × 16°, and the 12-μm size of the pixels established the physical dimensions of the optics. To maximize reliability, we chose not to use an adjustable focus for Pancam. Because the most important uses of the instrument involve imaging distant targets, we optimized the optical design for good focus at distance, accepting some defocus blur in the near field.

[21] The choice of stereo separation distance was also driven by the importance of far-field imaging. Small stereo separation provides good convergence angles for nearby targets, while large separation provides good ranging accuracy for distant targets. Because the more closely spaced (and lower resolution) Navcams and Hazcams are available for near-field ranging [*Maki et al.*, 2003], we chose to place the Pancam cameras as far apart as packaging restrictions allowed (30 cm) to maximize the accuracy of far-field ranging.

[22] We chose compact filter wheels as the simplest way to provide multispectral imaging capability. Practical considerations of filter wheel size led us to an eight position

filter wheel design for each camera. Because the Pancam science objectives include study of atmospheric aerosols, we devoted two of the 16 filter slots (one in each camera) to neutral-density red and blue filters that allow direct imaging of the Sun and hence direct determination of atmospheric opacity. This decision also enabled Pancam to be used by the rover to locate the Sun for navigation purposes, making it unnecessary to include a separate dedicated Sun camera on the vehicle. Three of the filters on the left Pancams were chosen to sample wavelengths close to the R, G, and B response of the human photopic function, so that true color images could be generated of the Martian surface scenery using methods similar to those outlined by *Maki et al.* [1999]. The left plus right pairs of red and blue filters also provide multispectral stereo imaging capability, with the red pair optimized for stereo imaging of high-contrast Mars scenes, and the blue pair providing an alternative method at a wavelength where topography is hypothesized to provide a larger source of scene contrast variations [e.g., *Kirk et al.*, 1999]. One filter position on Pancam was left empty to provide maximum imaging sensitivity at low light levels during night and twilight and to allow very short exposure times to be obtained during preflight testing at ambient or higher temperature conditions when dark current would normally prevent high signal to noise ratio imaging.

[23] The remaining filters for Pancam were chosen to detect and assess absorption features and the degree of crystallinity of the primary iron-bearing silicates and the secondary weathered iron oxides and oxyhydroxides that have been previously detected or inferred on Mars by telescopic and spacecraft remote sensing studies (see reviews by *Soderblom* [1992], *Roush et al.* [1993], *Bell* [1996], and *Morris et al.* [2000]). Specifically, the filters were chosen to sample (a) the near-UV to visible ferric absorption edge from ~440 to 750 nm, the slope of which has been shown to be an indicator of ferric mineral crystallinity [e.g., *Morris et al.*, 1985, 2000], (b) two crystalline ferric oxide absorption features typically centered near 650 nm and 860–900 nm, which have specific band centers that are diagnostic of oxide versus oxyhydroxide compositions [e.g., *Morris et al.*, 1985], and (c) the short wavelength wing of the classic "1 μm" absorption band in ferrous silicates like pyroxene, which has a band shape and position that can be diagnostic of the specific pyroxene (Ca, Fe, Mg) chemistry [e.g., *Adams*, 1974; *Cloutis et al.*, 1986]. An example of the wavelengths of the Pancam band passes overplotted on some spectra of typical ferric and ferrous minerals that could be expected to be detected on Mars is presented in Figure 2. The Pancam filter wavelengths are very close to those used by the IMP camera [*Smith et al.*, 1997a], allowing direct cross comparison between spectral units identified at the MER landing sites with those identified at the Mars Pathfinder landing site.

[24] Because Pancam generates far more data than the rest of the instruments on the Athena payload combined, we devoted considerable attention to the problem of data compression. We chose the JPL-provided ICER (wavelet) and LOCO (JPEG-like) compression algorithms [see *Maki et al.*, 2003], which provide good combinations of performance and speed when executed on the rover CPU in flight software. We also included subframing and downsampling capabilities in the design as a way of further controlling data volume.

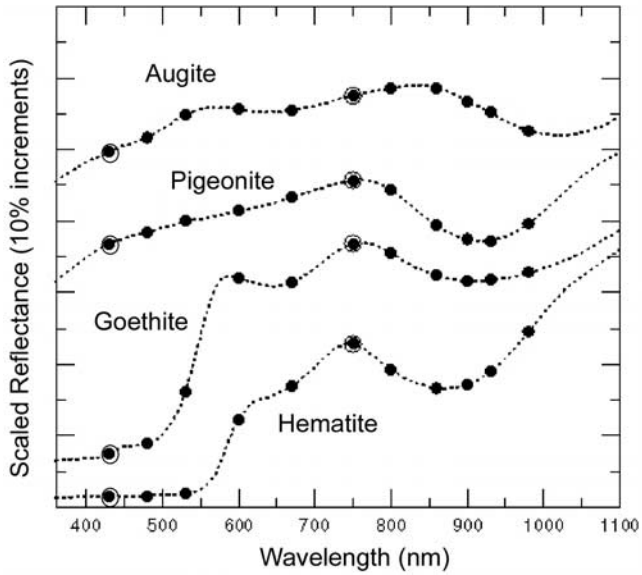

Figure 2. High-resolution lab spectra of two ferric oxides (hematite: αFe_2O_3 and goethite: $\alpha FeOOH$) and two ferrous silicates (augite: high Ca pyroxene and pigeonite: low Ca pyroxene) convolved over the 11 unique wavelengths of the Pancam "geology" filters (solid circles). The red and blue stereo filter positions are also indicated with open circles. The mineral spectra are offset relative to each other by 10%.

3. Instrument Description

[25] The Pancam system is a PI-lead science instrument that was designed by members of the Athena science team in cooperation with engineers and scientists at the Jet Propulsion Laboratory (JPL) and Ball Aerospace. Pancam components were constructed by JPL, Ball, and many other vendors, and fabrication and integration of the system occurred at JPL. The primary instrumental characteristics of Pancam are summarized in Table 3.

3.1. CCD and Electronics

[26] All nine cameras on each MER rover, plus the descent imaging system on each lander, use a common and nearly identical set of detectors and electronics. Each MER camera, including Pancam, utilizes a 1024 × 2048 frame transfer Charge-Coupled Device (CCD) detector designed by JPL and fabricated by Mitel (now DALSA Semiconductor, Inc). The CCDs are front-side-illuminated, buried-channel devices configured to use one half of the pixels (1024 × 1024) as the active imaging area, and the other half as a storage/readout area masked from illumination by an opaque black-painted aluminum light shield (Figure 3). The CCDs do not use UV-enhancing or antireflection coatings. There are no antiblooming structures built into the MER CCD pixels, but blooming is modestly controlled using a "clocked antblooming" technique that consists of transferring charge between two phases in the same pixel during the integration time. There is also a drain structure that runs along side the serial register that is used

Table 3. Pancam Instrument Characteristics

	Characteristics
	Mechanical/Environmental
1	two independent digital CCD cameras;
2	30 cm stereo separation, 1° toe-in;
3	mast-mounted, 1.54 m above surface;
4	360° azimuth and ±90° elevation actuation;
5	mass of each camera: ~270 g;
6	typical power consumption ~3 W per camera;
7	operating temperature within specs: −55°C to +5°C;
8	onboard calibration target, fiducial marks;
9	each camera has an eight position filter wheel;
10	uses ICER (wavelet) and LOCO (JPEG) compressors
	Optics
1	three element Cooke triplet lens design (G. Smith);
2	43 mm focal length, *f*/20 system;
3	<0.01% F tanθ geometric distortion;
4	optimal focus: 3 m; focus range: 1.5 m to ∞;
5	IFOV = 0.273 ± 0.003 mrad/pixel; FOV = 16° × 16°;
6	equivalent to a 109 mm lens on a 35 mm camera;
7	eight narrowband interference filters each (Omega Optical);
8	sapphire window for dust protection;
9	external sun shade, internal stray light baffles;
10	boresight calibrated with Navcams, Mini-TES
	CCD
1	1024 × 2048 Mitel (DALSA) frame transfer CCD;
2	12 μm square pixels, 100% fill factor;
3	opaque Al shield over storage region;
4	full well capacity = 170,000 ± 20,000 e^-;
5	system gain = 50 ± 3 e^-/DN;
6	system read noise = 25 ± 5 e^- at −55°C;
7	SNR ≥ 200 in all λ's at 50% full well;
8	absolute radiometry ≤7%, relative ≤1%;
9	dark current @ 27°C = 1.5 nA/cm^2;
10	dark current spatial nonuniformity <5%;
11	linearity >99% from 10 to 90% full well;
12	flatfield spatial nonuniformity <1%;
13	32 "reference" bias pixels outside of imaging area;
14	CCD frame transfer time = 5.2 ms;
15	CCD readout rate = 200 kpix/s (5.2 s);
16	integration time: 0–335 s, Δ = 5.12 ms;
17	subframing, downsampling, 4 × 1 row binning options
	Calibration target
1	8 × 8 cm base, 6 cm high post, 60 g mass;
2	three RTV rings with 20, 40, 60% reflectivity;
3	four RTV pigmented corner patches for color calibration;
4	vertical post casts shadow across all three rings to characterize diffuse versus direct illumination;
5	two mirrored annuli reflect sky color;
6	fully illuminated by the Sun from at least 10:00 a.m. to 2:00 p.m. LST for nominal rover orientations;
7	target is embellished with motto, markings, and drawings to be a "Mars sundial" for E/PO activities

to rapidly remove charge from the array during fast transfer or windowing. While these methods are not as effective as having true antiblooming structures in each 12 μm square pixel, they do not impact fill factor or collection efficiency, both of which are important for meeting Pancam measurement objectives.

[27] When powered, the CCD is constantly running in a "frame flush" mode where charge is drained from the array every 5.1 ms. An exposure is initiated at the start of a new frame flush cycle. Photons are then collected in the imaging area during the specified integration time (from 0 to 65535 exposure counts, where each exposure count equals 5.12 ms) and then once the exposure is complete the accumulated charge is rapidly shifted (shift time = 5.12 ms) into the storage area. This rapid charge transfer obviates the need for a mechanical shutter on the camera, but also limits the minimum exposure time (0 counts) to 5.12 ms and leads to the generation of frame transfer smear signal that must be corrected in calibration (see section 4.2.4 below). Once the collected photons are in the storage area, they are clocked out, row by row, into a horizontal serial register for

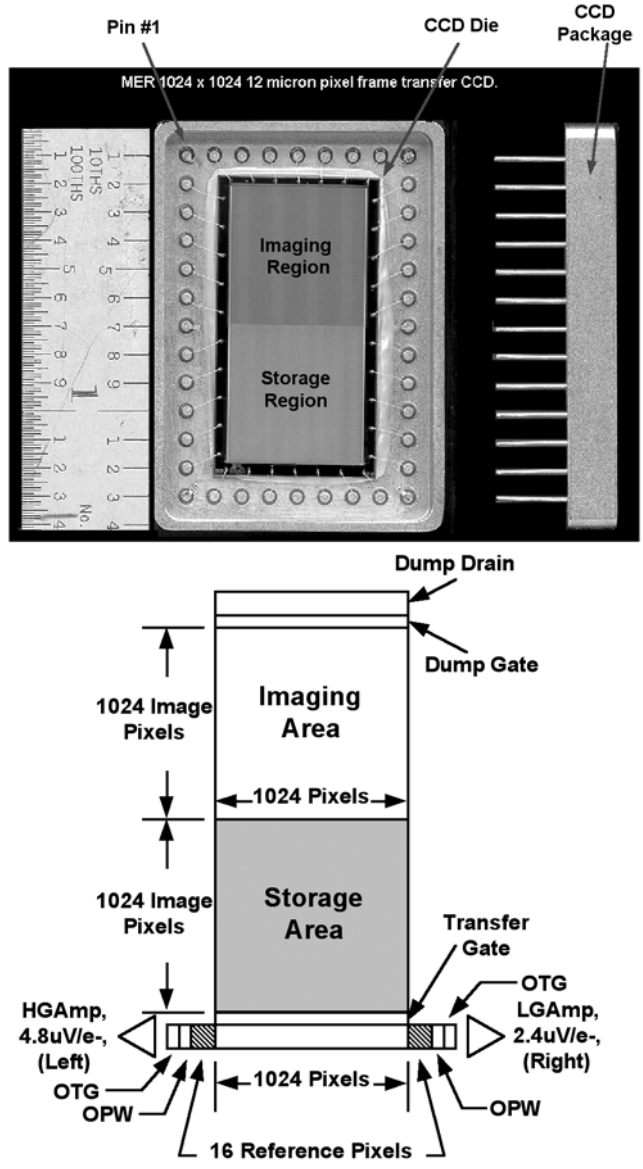

Figure 3. MER CCD package and schematic representation.

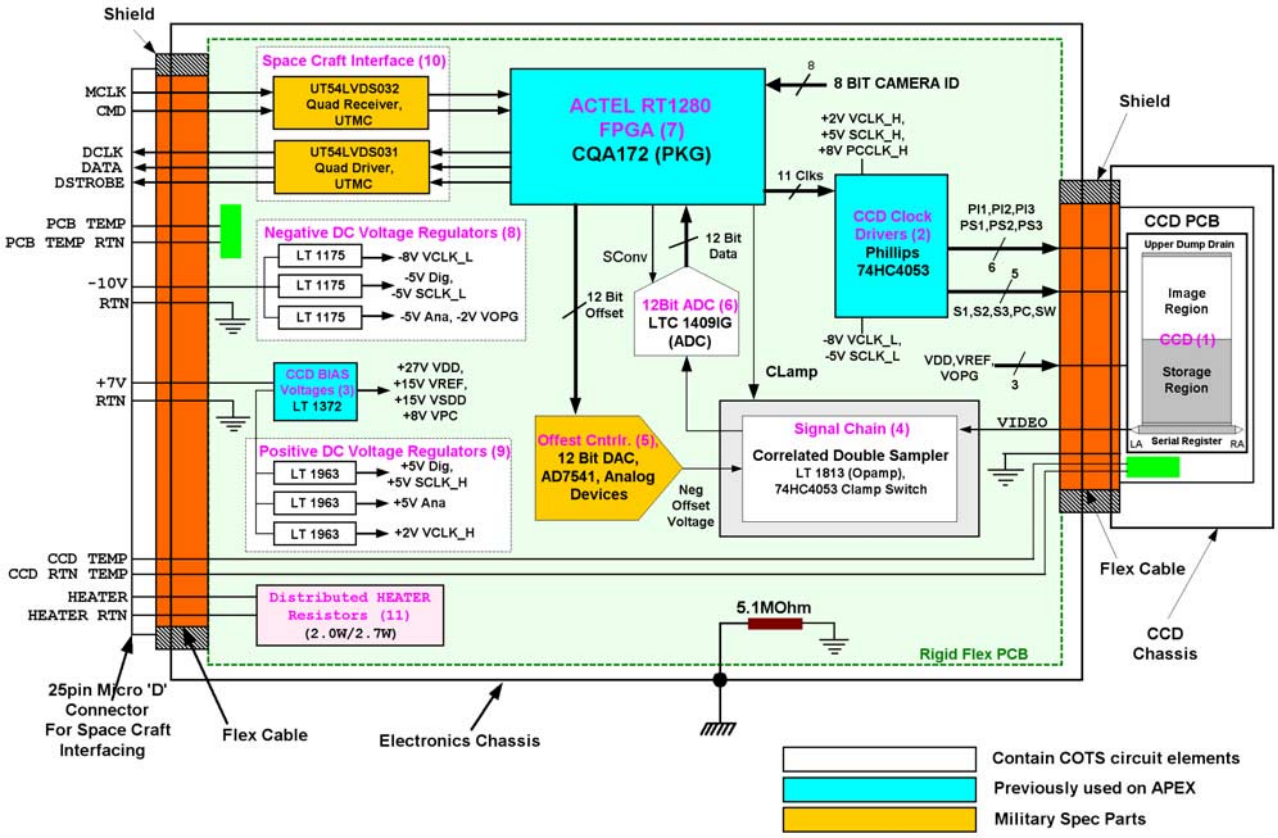

Figure 4. MER camera electronics block diagram.

subsequent amplification and digitization. The readout rate is 200 kHz (200,000 pixels/s), or 5 ms per row, leading to a total readout time of approximately 5 s per full frame image. The horizontal register also contains 16 extended or "reference" pixels at each end that are also read out and digitized by the camera electronics (Figure 3). These pixels provide information on the video offset (bias) level, and can be optionally saved for downlink as a 32 × 1024 "reference pixel" Experiment Data Record (EDR) image file (see also *Maki et al.* [2003] for additional information on data product naming and organization).

[28] The MER camera electronics (Figure 4) consist of clock drivers that provide three phase timing pulses for transfer of charge through the CCD, as well as a signal chain that amplifies the CCD output and converts it from analog voltages to a 12-bit digitized signal. An Actel Field Programmable Gate Array (FPGA) provides all of the timing, logic, and control functions in the signal chain. The FPGA also inserts a unique camera identification number into the telemetry for each camera to simplify data management and postprocessing. A correlated double-sampling Analog-to-Digital Converter (ADC) compares the amplified CCD output voltage against a (commandable) reference voltage from the FPGA to achieve 12-bit (0–4095) digitization of the signal. Gain, read noise, and other performance metrics of the Pancam signal chain are reported below. Similar information for the other MER cameras is reported by *Herkenhoff et al.* [2003] and *Maki et al.* [2003]. Additional details on the MER camera CCDs and electronics can be found in the calibration report of *Bell et al.* [2003b].

3.2. Optics

[29] The science and measurement requirements outlined above (spatial resolution, depth of field, and field of view), the realities of limited payload mass and volume resources, and the harsh Martian surface environmental conditions all dictate design constraints on Pancam optics. The resulting design is small (short focal length), lightweight, has a slow focal ratio (greater depth of field), employs discrete

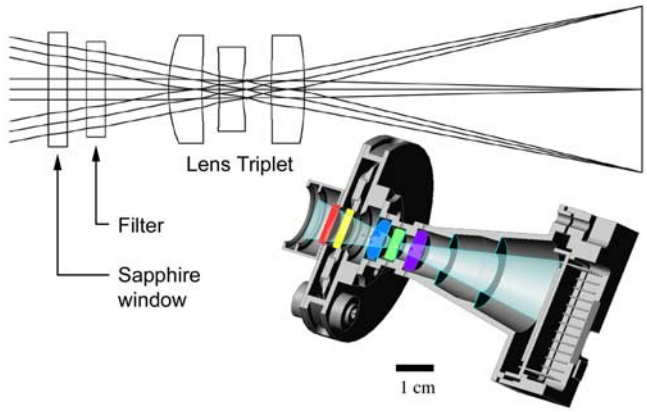

Figure 5. (top) Pancam optics schematic and (bottom) CAD cross-sectional view.

spherical or flat elements rather than cemented or aspherical surfaces, and does not allow vignetting of the field. An antireflection coated sapphire window protects the filters and filter wheel mechanisms from contamination by airborne dust particles and helps cut down stray and scattered light effects. A short sunshade and set of black internal baffles provide rejection of stray and scattered light. The Pancam lens design is a Cooke triplet as shown in the layout in Figure 5. The lens was designed to have a focal length of 43 mm, which yields a field of view (FOV) of 16° × 16° (22.5° on the diagonal) that is approximately equal to the FOV of a 109 mm telephoto lens on a standard 35 mm camera. IFOV of each pixel was designed to be approximately 280 × 280 μrad, yielding 560 μrad limiting resolution on a pair of adjacent 12 μm pixels, or a Nyquist limit for spatial frequency detection of 41.67 cycles/mm. The lenses were designed to operate at *f*/20 with a fixed (hyperfocal) distance of 3.0 m and to view objects in focus whose distances range from infinity to 1.5 m (the depth of field). The Modulation Transfer Function (MTF) performance of the optics was assessed at the component level at three wavelengths: near the shortest Pancam band pass around 430 nm, near the peak of the planet's spectral reflectance function at 750 nm, and near the longest Pancam band pass at 980 nm. At 430 nm, the actual MTF values cluster just below the diffraction-limited value of 55% at the Nyquist cutoff frequency. Similarly, for 750 nm, the actual curves cluster just below the diffraction limit of 25% at Nyquist. And for 980 nm, the curves drop to just below the diffraction limit of 8% at Nyquist. Major characteristics of the Pancam optics are summarized in Table 3. Additional details on the Pancam (and other MER camera) optics design and component level performance can be found in the paper of *Smith et al.* [2001].

3.3. Filters

[30] Each Pancam camera is equipped with a small eight position filter wheel, providing the only multispectral imaging capabilities for each rover. Fifteen of the 16 filter wheel slots contain filters; one slot (L1) was left empty to maximize sensitivity during low-light and ambient Earth temperature (preflight) imaging conditions. The filters are glass interference filters, 11 mm in diameter (10 mm clear aperture) and were fabricated by Omega Optical, Inc. Thirteen of the 15 filters per camera pair are so-called "geology" filters, designed for imaging of the surface or sky, and the remaining two filters are "solar" filters, designed for direct imaging of the Sun. The geology filters were designed and fabricated to have peak transmission >85%, transmission ripple within the passband of <10%, central wavelength uniformity and central wavelength shift resulting from angle of incidence variations across the FOV of <1%, and a wavelength-integrated rejection band response in the 400 to 1100 nm region of <1% of that filter's integrated in-band response. The solar filters have the same requirements for their band passes, but also are coated with metallic attenuation films to provide an additional factor of 10^5 reduction in overall transmission. The shortest wavelength (440 nm) and longest wavelength (1000 nm) filters are actually short-pass and long-pass filters, respectively, to provide wider band passes to maximize the SNR at these extreme ends of the CCD spectral response profile (see Figure 12). The filters are divided between the cameras so that, in general, the shorter wavelength filters ≤750 nm are in the left camera and the longer wavelength filters ≥750 nm

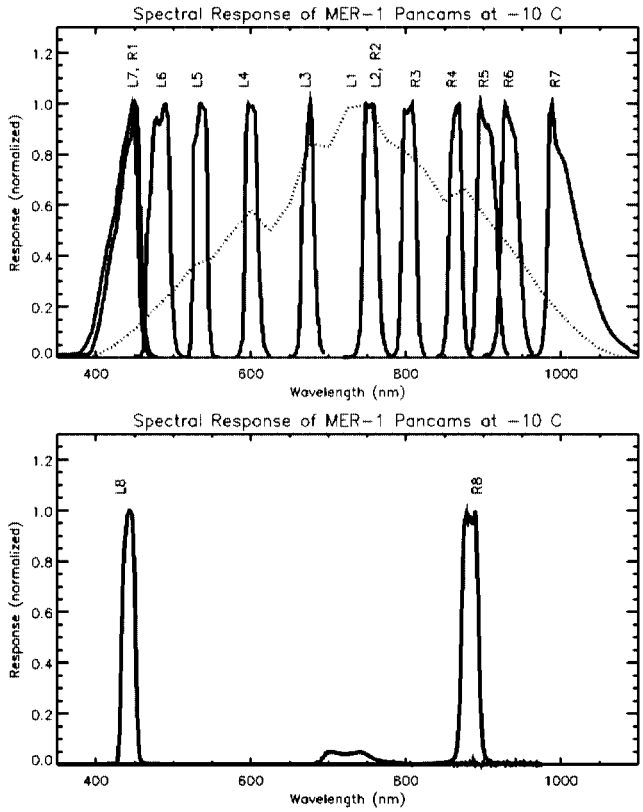

Figure 6. Pancam (top) geology filters and (bottom) solar filters normalized transmission profiles. All of the data plotted represent the total system throughput, but the solar filter response increase do not include the effects of the neutral density (ND) coatings. The solar filter response increase near 700–750 nm is a red leak in the blue solar filter (L8) that may contribute substantial red light to the blue solar filter flux. Additional characterization of the magnitude of this red leak is ongoing.

Table 4. Pancam Filter Characteristics

Name	λ_{eff}, nm	Band Pass, nm	Comment
	Left Camera		
L1	739	338	empty slot, no filter
L2	753	20	red stereo L
L3	673	16	geology
L4	601	17	geology
L5	535	20	geology
L6	482	30	geology
L7	432	32	blue stereo L
L8	440	20	solar ND5
	Right Camera		
R1	436	37	blue stereo R
R2	754	20	red stereo R
R3	803	20	geology
R4	864	17	geology
R5	904	26	geology
R6	934	25	geology
R7	1009	38	geology
R8	880	20	solar ND5

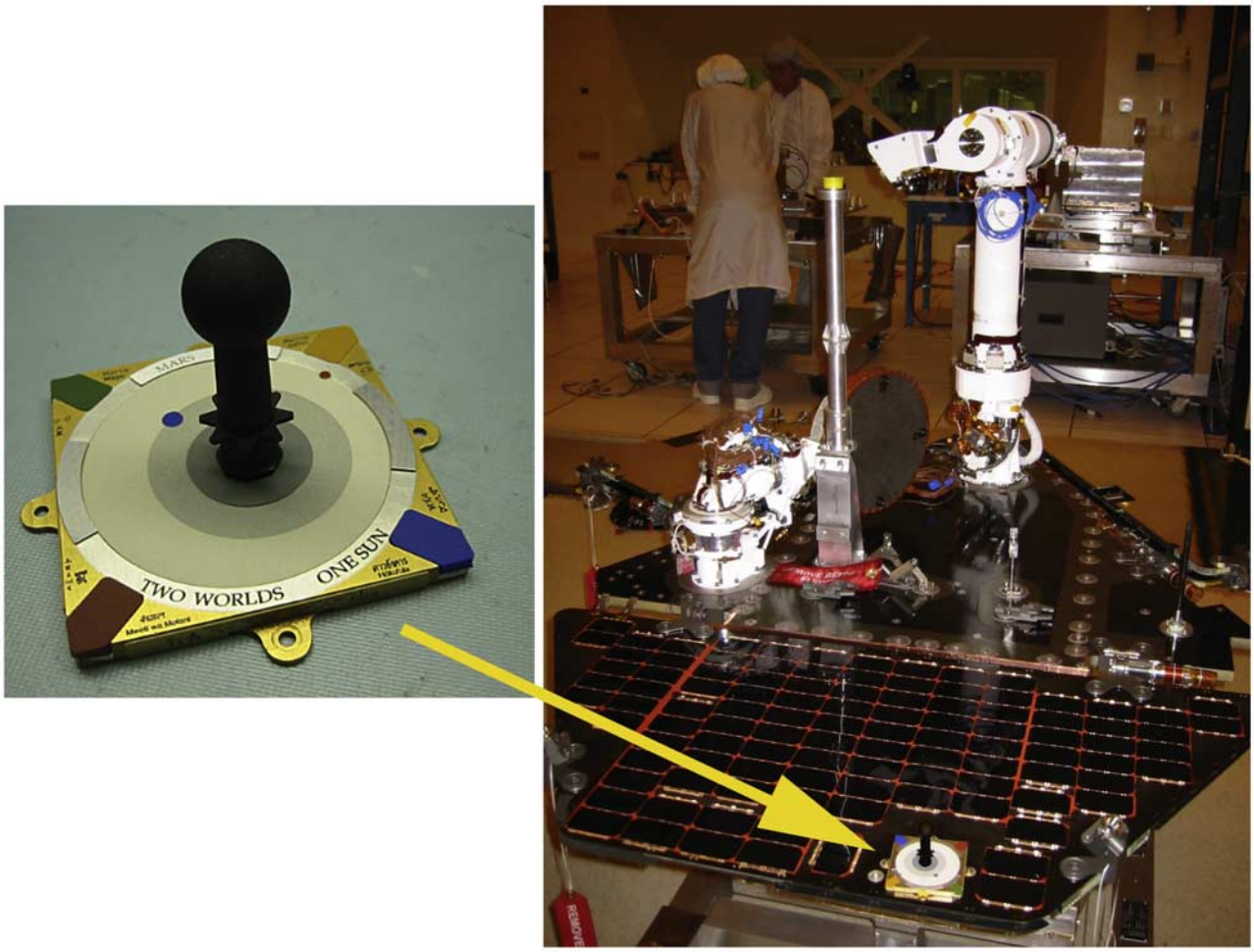

Figure 7. (left) Pancam calibration target, with (right) its position on the rover's -X solar panel indicated. The target has an 8 × 8 cm square base and the black shadow post is 6 cm high. The target is ~135 mm from the cameras when they are pointed at it, and it is viewed by the cameras at a fixed emission angle of ~53.5 ± 2.5° from the axis normal to the solar panels. The Pancam mast assembly (PMA) is the white tube on the side of the rover equipment deck opposite the calibration target (the PMA camera bar is pointed down in this image).

are in the right camera. Two filters, near 440 and 750 nm, are redundant in the left and right Pancams. This provides stereo imaging capability in two colors, as well as redundancy for generating pseudo-true color images in the right Pancam, in the event of a left Pancam failure. Central wavelength and band-pass information for the Pancam filters are listed in Table 4. A plot of normalized Pancam filter band passes is provided in Figure 6.

3.4. Calibration Target

[31] Each rover carries a specially designed calibration target (Figure 7) to verify and validate the preflight calibration of the Pancam imaging system and to monitor the stability of the calibration during the mission. The requirements for location of this target were (a) location with an unobstructed view of both Pancam camera heads when the Pancam and PMA are in the deployed configuration; (b) maximum distance from the cameras for best focus; (c) maximum likelihood that it will be fully illuminated by the Sun between at least 10:00 a.m. and 2:00 p.m. LST; and (d) minimization of diffuse or reflected sunlight from rover structures that could provide "contamination" illumination onto the target.

[32] The targets are based on the successful "post and bulls eye" calibration targets used by the IMP investigation [*Smith et al.*, 1997a; *Reid et al.*, 1999], but have been modified somewhat based on Pathfinder experience. Each target is 8 × 8 cm square with a 6 cm high black vertical post for casting a shadow. Measurements in and out of the shadowed region provide a way to quantify the direct versus diffuse components of incident scene radiance [*Reid et al.*, 1999; *Thomas et al.*, 1999]. The surface of the calibration target contains three gray level annuli of 20%, 40%, and 60% reflectivity ("black," "gray," and "white" rings, with the white ring farthest from the post), four pieces of pigmented "color chip" materials in the corners, and two partial annuli of polished aluminum to reflect the color of the Martian sky. The calibration target materials consist of silicone RTV (GE RTV655) pigmented with either titanium dioxide or carbon black to raise or lower the reflectivity, or submicron powders of hematite, goethite, chromium oxide, or cobalt aluminate to generate the red, yellow, green, and

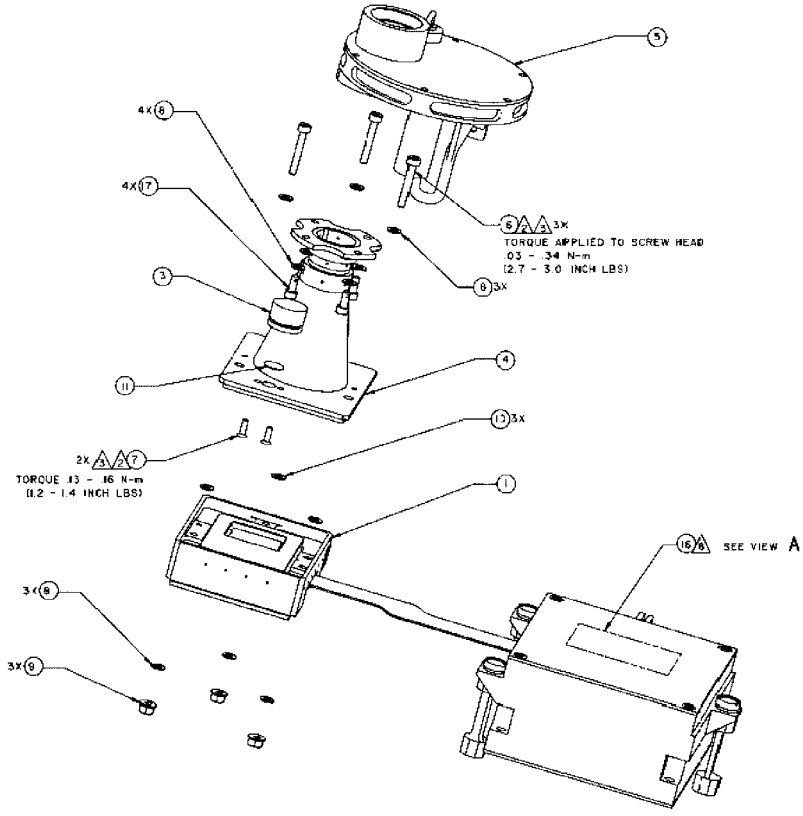

Figure 8. Schematic assembly drawing of the Pancam. Major components include the filter wheel assembly (labeled 5), the Pancam optics barrel assembly (4), the CCD housing (1), and the separate electronic box assembly (16). This is a portion of JPL Pancam assembly drawing 10212720.

blue color chips, respectively. The materials were UV-irradiated for the equivalent of 30 Martian sols to minimize any UV-degradation of the reflectance levels during operations on the Martian surface. Sheets of the calibration target rings and color chip materials were fabricated by D. Britt using the same process that was used to generate similar materials for the IMP calibration targets [*Smith et al.*, 1997a; *Reid et al.*, 1999].

[33] In addition to providing calibrated reflectance and color surfaces that will be used to validate, monitor, and refine Pancam calibration on Mars, the calibration targets also serve an education and public outreach (E/PO) role in the mission, as each is being used as a "Martian sundial" to help demonstrate the concepts of seasons, timekeeping, and planetary rotation to school children. To that end, the surface and sides of the calibration target have been embellished with a place and date ("Mars 2004") and motto ("Two Worlds, One Sun"), as is the tradition for sundials. The outer edges of the white and gray rings have been sized to accurately represent the orbits of Mars and Earth, and representations of both planets have also been positioned on the rings with small blue and red color chip dots. The word "Mars" has been etched onto the surface in 16 additional languages, and the sides of the target contain drawings by school children and an inspirational message for any future travelers who may venture to the MER landing sites one day.

[34] The Pancam calibration target is located on the -X (rear) solar panel of each rover, at a distance of approximately 135 mm from each camera (when the cameras are pointed at a PMA azimuth of 3.04 radians (174.2°) and an elevation of −0.678 radians (−38.8°). The target is viewed by Pancam at a fixed emission angle of approximately 53.5° ± 2.5° relative to the axis normal to the rover solar panels (Figure 7). Although the targets will be imaged at less than the optimal 1.5 m minimum focus distance, the resulting defocusing is minor and the calibration target surfaces were intentionally oversized to compensate for this effect.

3.5. Mass, Power, Data, and Environment

[35] The total mass of each Pancam camera, including filter wheel and electronics box, is 267 g. The mass of the calibration target is 68 g. Each camera requires +7.1V and −10.4V from the rover power supply, and power usage during full-frame imaging is 1.4 W (idle), 2.4 W (integration and readout), and 3.8 W maximum (during CCD fast flush). Each full-frame image generates 12.98 Mbits of data (a 1024 × 1056 stream of 12-bit pixels, including reference pixels). The data are passed to the rover Flight Software (FSW) for possible postprocessing (see section 5.3 below) and then packetized for telemetry downlink. The FSW allows the acquisition of left and right camera images simultaneously, but any subsequent onboard image processing is performed in series.

[36] Pancam is designed to operate within calibrated specifications on Mars when environmental temperatures are between −55°C and +5°C. The CCDs themselves can operate safely at temperatures between −110°C to +45°C, but they will not formally be within calibrated specifications

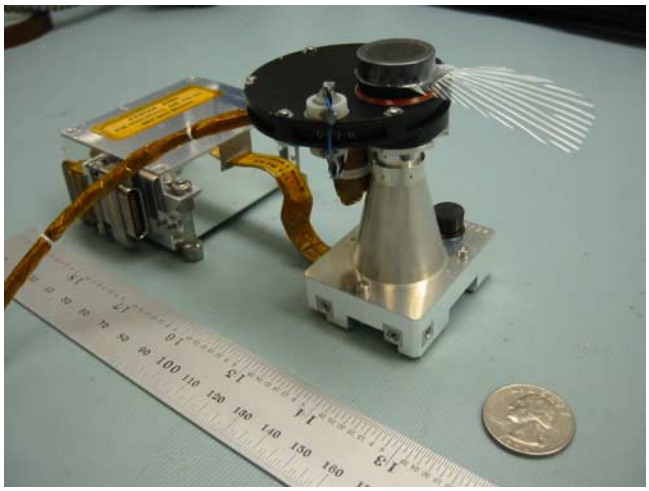

Figure 9. An assembled flight Pancam instrument prior to mounting on the Pancam mast assembly camera bar. The CCD/optics/filter wheel assembly is in the foreground, and the electronics box is in the background. The mylar cover over the sunshade baffle was for dust/contamination protection during laboratory testing only.

outside of −55°C to +5°C. The filter wheels can operate only between −60°C to +45°C, and the electronics only between −60°C to +55°C. The minimum recommended nonoperating (survival) temperature for all components is −110°C, and the maximum is +55°C. Each Pancam CCD and the left Pancam electronics box are equipped with a temperature sensor. A small 3.5 W (maximum) strip heater is attached to each electronics box and filter wheel to provide survival and warm-up heating if required. Because of power limitations, the CCDs themselves are not controlled to a fixed operating temperature but will drift with time during each sol on Mars. Therefore knowledge of the CCD and electronics temperatures is required for proper calibration of Pancam images.

3.6. Integration and Articulation

[37] Each Pancam camera consists of a separate electronics box and CCD/optics/filter wheel assembly that are connected by a flex cable (Figure 8). The two Pancam cameras (Figure 9) on each rover are mounted on a visor-like camera bar (Figure 10) along with the two Navigation

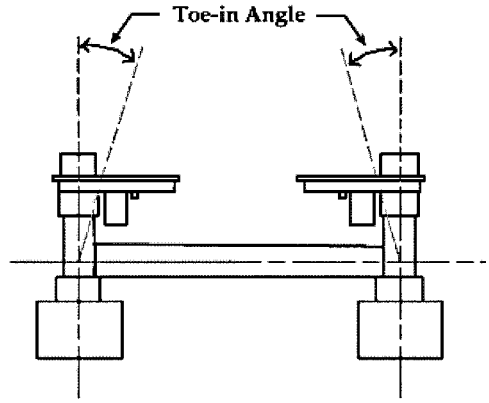

Figure 11. Schematic representation of the Pancam toe-in angle. The camera separation is 300 mm and the toe-in angle is 1°. The diagram is not to scale; the camera boresights are actually aligned along the toed-in dashed lines.

cameras (Navcams; [*Maki et al.*, 2003]), and the camera bar is mounted atop the PMA (Figure 7), which provides the ability to point the cameras from 0° to 370° in azimuth and −104° to +90° in elevation [*Squyres et al.*, 2003]. By convention, the "left" cameras are on the left side of the bar as seen by a viewer standing behind the camera bar. When the PMA is deployed and the camera bar is positioned in its nominal horizon-viewing elevation (0°), the Pancams will be approximately 1.5 m above the Martian surface. The separation between the two Pancam cameras is 30 cm, which will yield hyperstereo images for scientific and navigation purposes (for reference, the stereo separation or interpupillary distance between human eyes ranges between about 5.4 cm and 7.2 cm). The cameras are not symmetric about the PMA azimuth rotation axis; the left Pancam is ∼13.5 cm from the axis and the right Pancam is ∼16.5 cm from the axis (Figure 1). The Pancams are toed-in relative to each other with a toe-in angle of 1° (Figure 11). Toe-in results in 100% image overlap at a distance from the camera proportional to the toe-in angle. For a 1° Pancam toe-in, this distance is approximately 10 m.

[38] During the cruise and entry, descent, and landing (EDL) phases of the mission, flexible metallic dust covers are held between the two outer baffles in the sunshade

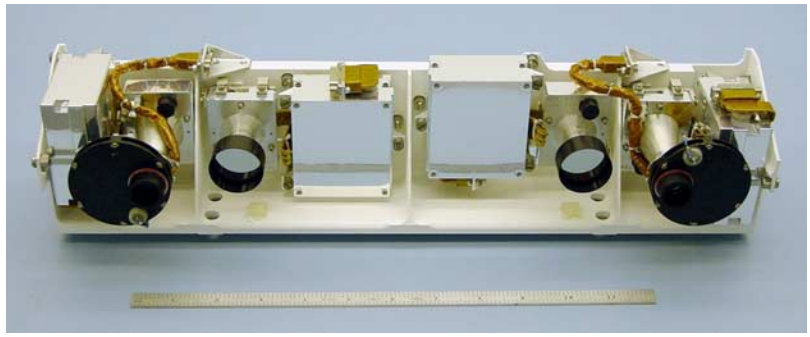

Figure 10. The MER PMA camera bar. The Pancams are the outer cameras (300 mm separation), and the Navcams are the inner cameras (200 mm separation). As viewed this way, the left Pancam and Navcam are on the right side of this picture, and the right cameras are on the left. The ruler in the foreground is 12 inches (30.5 cm) long.

(Figure 5) to guard against dust contamination of the sapphire window during airbag impact, roll, and deflation. These EDL dust covers are designed and tested to pop out permanently (and gracefully) the first time the camera bar is deployed on the PMA. After they pop out they remain attached by a short lanyard to the camera bar, but out of the field of view of any of the PMA cameras.

4. Instrument Performance and Calibration

4.1. Test Procedures and Conditions

[39] A rigorous test and calibration program [*Bell et al.*, 2003a] has been conducted to derive and monitor Pancam instrument performance and calibration parameters and to validate the instrument calibration pipeline. These tests were conducted at the individual component level (CCDs, filters), at the assembled (standalone) camera level for each flight unit, at the subsystem level when the cameras were integrated with the camera bar and PMA, and finally at the system level during fully assembled rover testing. Tests were performed at both (Earth) ambient temperature and pressure conditions and under thermal vacuum conditions simulating the range of expected conditions on Mars. The most critical flatfield, throughput, and responsivity, calibrations were performed under near-vacuum ($P \leq 10^{-6}$ torr) and at three temperatures ($-55°C$, $-10°C$, and $+5°C$) chosen to bracket the nominal daytime range of surface conditions expected during the mission. Coalignment tests among Pancam, Navcam, Hazcam, and Mini-TES were conducted in ambient conditions and in near-vacuum at temperatures of $-95°C$, $-55°C$, $-30°C$, and $0°C$.

4.2. Component Level and Camera Standalone Tests and Results

4.2.1. CCD QE

[40] The quantum efficiency (QE) of a typical Pancam CCD measured prior to its integration into a camera is shown in Figure 12 at two temperatures that bracket the range over which Pancam is radiometrically calibrated. The nature of this QE curve is typical for silicon-based CCD detectors, and the $\pm 2-3\%$ variations in QE across the expected temperature range provided the motivation for obtaining radiometric calibration data at the subsystem level at three temperature set points ($-55°$, $-10°$, and $+5°C$). As described below and by *Bell et al.* [2003b], the temperature dependence of the Pancam system responsivity is smooth and well behaved as a function of temperature. The relatively low QE at the extreme ends of the spectral response is somewhat mitigated by the use of wider passband filters at these wavelengths (Figure 6).

4.2.2. Gain, Read Noise, Full Well, Linearity, and Digitization

[41] The system gain (e^-/DN), read noise (e^-), and full well capacity (e^-) of each MER CCD were determined using the photon transfer method of *Janesick et al.* [1987]. Representative results are shown in Figure 13. The Pancam system gain target was 50 e^-/DN in order to provide optimized digitization of the 12-bit (4095 DN) dynamic range of the ADC over the expected 150,000 to 200,000 e^- full well capacity of the CCD. Data obtained during CCD component-level calibration show that the average measured gain of the flight Pancams is 50 ± 3 e^-/DN, and the average measured full well capacity is $170{,}000 \pm 20{,}000$ e^-. Read noise was measured at the CCD component level during parts screening and was found to average 7 ± 1 e^- for all MER science CCD candidates. Although the system gain setting is much higher than the noise floor of the CCD, it was judged to be acceptable because Pancam will be used for bright scene imaging (the Martian terrain), and thus the photon (shot) noise of these images, which goes as the square root of the number of photons detected, will typically be higher than 50 e^-, allowing the image noise to be resolved. Photon transfer measurements of the assembled flight cameras reveal that the total system read noise (including ADC digitization and other electronics noise sources) is 60 ± 5 e^- at $+20°C$ and falls to 25 ± 5 e^- at $-55°C$. These values are ≤ 1 DN. The gain and the full well were found to vary linearly by $5-10\%$ between room temperature and $-110°C$ (this is part of the reason for the need to characterize the temperature dependence of the radiometric calibration coefficients in section 4.2.10 below). Photon transfer tests were also used to assess the linearity of the CCD and camera system. Regression analysis showed that all MER flight cameras respond linearly to incident illumination, with an average r^2 linear correlation coefficient >0.999. None of the 8,388,608 active plus shielded pixels on the four flight Pancams were found to be "dead". Some nonlinear or otherwise "hot" or "gray" pixels were identified, but they are exceptionally rare for these cameras; most of them occur in columns 1 or 1024 (see below).

[42] Data from each MER CCD are digitized by comparing the input signal from a CCD pixel to a reference voltage (V_{ref}). The comparison is done by dividing V_{ref} by a network of adjustable resistors until it compares with the input voltage to within $V_{ref}/4096$. In the specific cases of DN values of 2^n, V_{ref} is divided by a single resistor. In order to smoothly transition from DN values of 2^n to DN values of

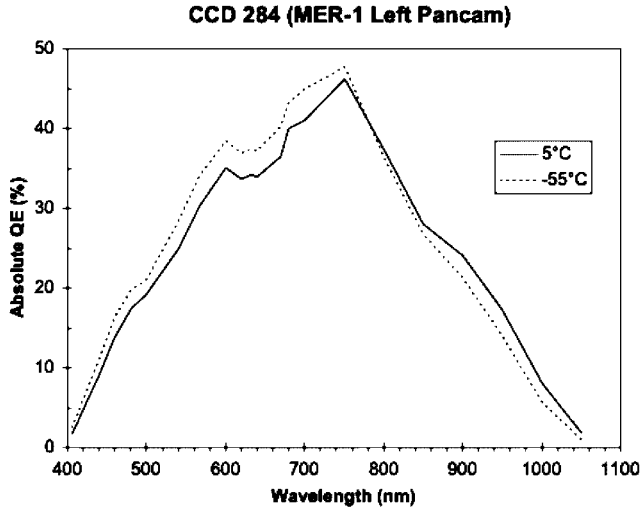

Figure 12. CCD quantum efficiency (QE) for flight device #284, the CCD used in the MER-1 left Pancam (camera serial number 114). The QE of this device is representative of that of all MER camera CCDs. The QE is shown at two temperatures that bracket the range over which Pancam is radiometrically calibrated.

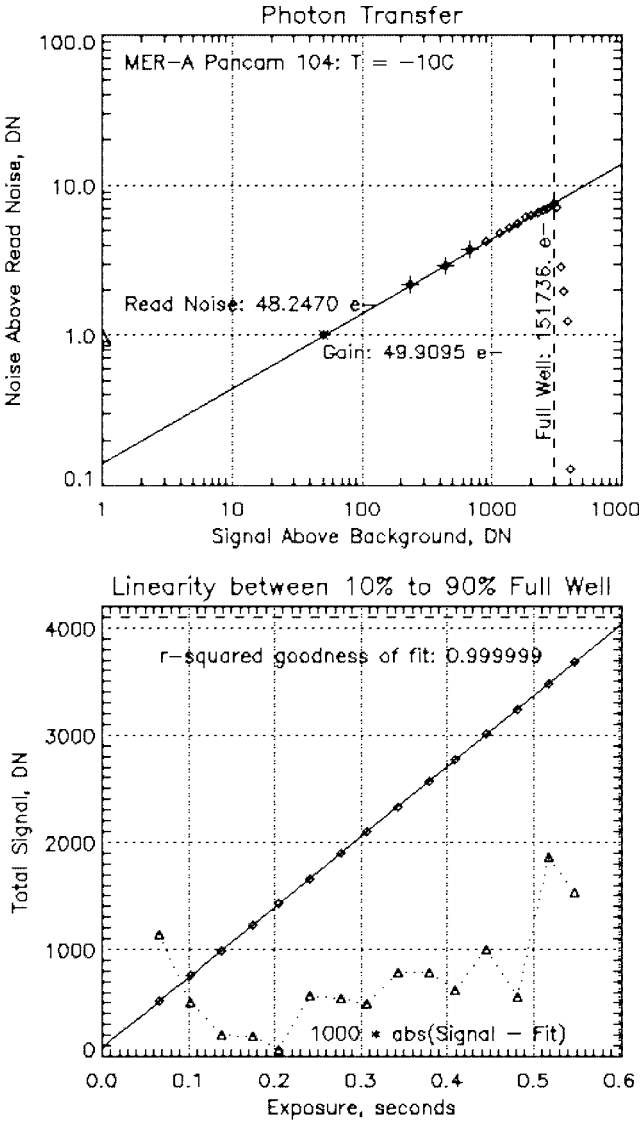

Figure 13. (top) Representative photon transfer and (bottom) linearity plots from MER-B left Pancam (MER-2 vehicle; camera serial number 104), measured at −10°C. The photon transfer analysis uses the methods defined by *Janesick et al.* [1987] to derive the gain, full well, and read noise characteristics of a CCD. The deviations from linearity for the MER camera CCDs are typically less than one part in 1000 (triangles, bottom plot).

$2^n \pm 1$, the network of resistors must match the single resistor to an accuracy of one part in 10^4, a feat difficult to achieve in practice. As a result, a phenomenon known as ADC uneven bit weighting is sometimes observed in CCD cameras like these [e.g., *Brown*, 1997]. The phenomenon can be seen in the histogram of an image with a broad range of DN values as a series of spikes (anomalously full histogram bins and anomalously empty ones) at or near certain DN values that are integer multiples of 2^n. As resistors are temperature sensitive, this error is also temperature dependent. We obtained adequate statistical samples of all DN values at a variety of temperatures during Pancam calibration, and are using these data to develop a correction for this effect as part of our standard data reduction pipeline. The phenomenon is only problematic for uncompressed or losslessly compressed data that is preserved in 12 bit format; therefore it will impact only a small fraction of the expected MER data. Fortunately, the phenomenon is still relatively minor, effecting only a few tens of DN values out of the entire dynamic range. Additional details are provided by *Bell et al.* [2003b].

4.2.3. Blooming

[43] As described above, there are no antiblooming structures built into the MER CCD pixels, and so some of the charge that accumulates after each pixel reaches its full well capacity can sometimes spread or "bleed" to other pixels. Experience shows that the effect is not a significant source of noise or image degradation for exposure levels below a few times the full-well level. Above that level, however, blooming of a small region of the image can produce signal bleed over a wide area. Intelligent choices of exposure times to guard against oversaturation will mitigate this effect during the mission, although occasional unexpected glints, especially off metallic structures on the rover itself, may produce some image degradation. No temperature dependence to the blooming was noted in tests conducted at +5, −55, and −85°C. Also, tests show that because of the CCDs efficient and high-speed charge flushing scheme, the effects of even massively oversaturated and bloomed images are not detectable in the next image obtained (the soonest possible next full-frame image can be obtained about 5 s later).

4.2.4. Frame Transfer Smear

[44] The MER CCDs operate as frame transfer devices without mechanical shutters. After the active region of the CCD has been exposed to light for the specified period, the charge in those 1024 × 1024 active area pixels is quickly transferred to the 1024 × 1024 pixel storage region under the opaque aluminum shield for subsequent readout. However, the frame transfer process is not instantaneous, and during the ~5.1 ms it takes to transfer the charge to the masked region, photons are still being collected in the active area. The end result is to induce an additional scene-dependent, linear (ramp) signal component on top of the desired image. This additional component is known in CCD imaging as frame transfer smear. Additionally, because an exposure is initiated at the start of a new frame flush cycle (see section 3.1 above), 5.1 ms of additional frame transfer smear is also added to each image prior to the start of the actual exposure.

[45] The frame transfer effect is zero in row 1 of the image (the last row to be flushed before the exposure and the first row that is almost instantaneously transferred into the storage region after the exposure), and is maximum in row 1024 (the first row to be flushed ~5.1 ms before the exposure and the last row transferred afterward, ~5.1 ms later). The magnitude of the effect is proportional to the ratio of the integration time divided by the ~10.2 ms total preexposure and postexposure frame transfer smear accumulation time. That is, for an image with an integration time of 10.2 ms, the frame transfer signal in the 1024th row of the image will be roughly double the actual, desired scene signal (that is, the contamination signal is 100%). Our signal to noise (SNR) requirement of SNR >200 for exposures >50% full well (Table 3) provide guidance on a minimum

exposure time for which frame transfer smear must be operationally corrected. Specifically, an SNR of 200 implies a noise threshold of less than 0.5%. A conservative operational approach, then, is to apply a frame transfer correction whenever the exposure time is less than or equal to 200 times the frame transfer smear accumulation time, or ~2000 ms, because then the worst-case smear level exceeds 0.5% of the scene signal somewhere in the image. For exposures longer than ~2 s, the frame transfer smear contamination component represents a statistically insignificant part of the detected signal, and testing has shown that it can usually be ignored without negative implications for analysis.

[46] Because of the linear nature of this "contaminating" signal, it can easily be removed in one of two ways: (a) a simple model can be constructed a posteriori that linearly subtracts a percentage of the scene signal from rows "downstream" in the readout process to analytically subtract the frame transfer component, or (b) a zero exposure time image of the same scene can be taken immediately before or after the nonzero exposure, and then it can be subtracted from the nonzero exposure to empirically remove the frame transfer smear component. Either implementation can be invoked as part of Pancam image processing (discussed in more detail below), and both implementations have been tested and validated as part of Pancam calibration activities. Pragmatically, since many Pancam exposure times are predicted to be in the hundreds of ms range (see below and Figure 18), and onboard correction is preferable over modeling after the fact, frame transfer smear correction will usually be applied by acquiring an associated zero image whenever possible.

4.2.5. Video Offset (Bias) Control

[47] Part of the operation of the MER CCDs involves a bias or offset voltage added to the signal chain by the FPGA to prevent undersaturation (zeros) and to most efficiently utilize the dynamic range of the ADC [*Bell et al.*, 2003b]. Nominally, the offset voltage is 2.5V, which corresponds to a user-selected video offset value of 4095 in the FSW. With this nominal video offset level, the bias level of Pancam images as measured by the reference pixels (see below) is targeted to range from approximately 20 to 40 DN. However, as the camera electronics box temperature gets colder, this bias level decreases as the circuit resistance changes, and under some imaging situations at the coldest temperatures the bias could "bottom out" at 0 (e.g., see Figure 14c). Lowering the video offset level raises the bias, thus preventing the signal from dropping to 0 under cold conditions. By design, lowering the video offset by N causes an increase in the bias level of 2N. That is,

$$\Delta\text{Bias} = 0.5(4095 - \text{Video Offset}). \quad (1)$$

Tests at ambient and over the expected range of Mars operating conditions show that the effect is linear and that the data match design expectations. Operationally, we will utilize a single default video offset value for all images from each camera, with the default value chosen to keep bias levels above ~10 DN even at the lowest expected operational temperatures (see Table 6). However, there may be special circumstances under which this commandable offset value needs to be lowered even farther, for example during nighttime imaging. Therefore care must be taken to query

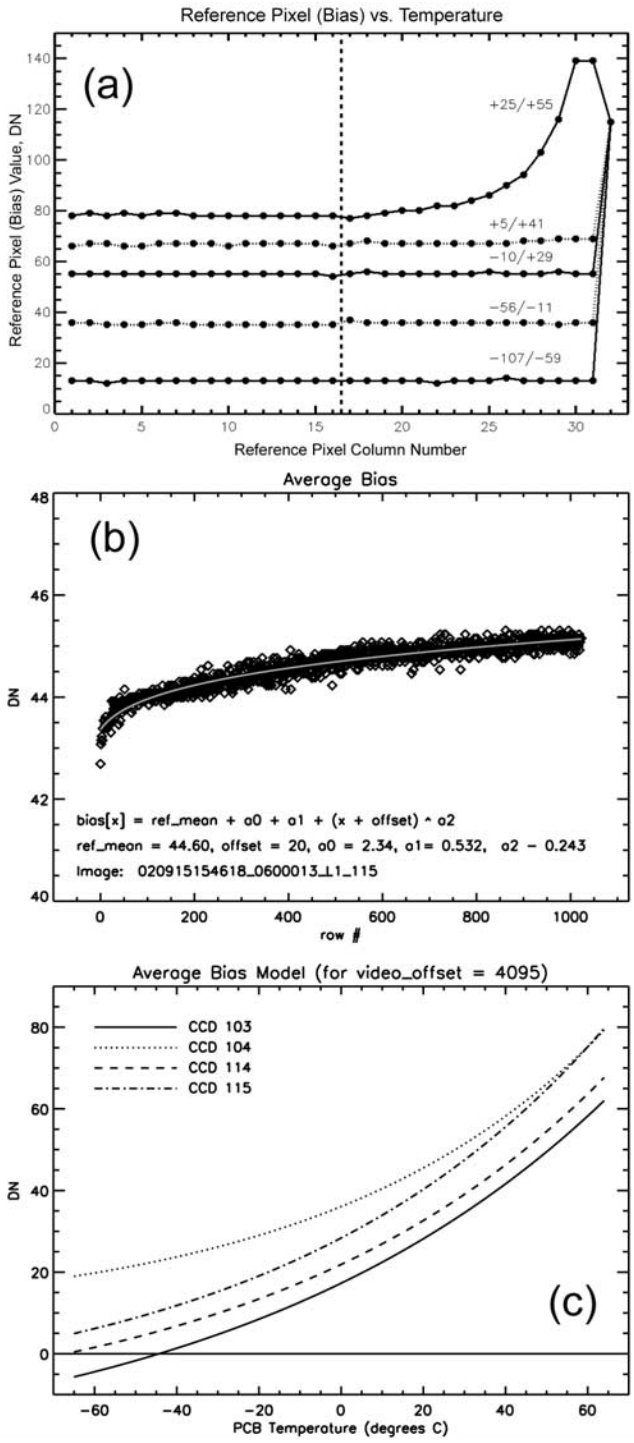

Figure 14. (a) Typical values of MER CCD reference pixels versus temperature. Pixels 1–16 are on the left side of the horizontal register, and pixels 17–32 are on the right. Pixel 32 is the camera ID (115 in this example), and pixel 31 is a copy of 30 (see text). The two numbers above each curve are the CCD and electronic box temperatures in °C. (b) Example of slow increase in MER CCD bias level caused by a small temperature increase of the electronics during the ~5 s image readout. (c) Average Pancam bias model value versus temperature for all four flight cameras.

Table 5. Pancam Preflight Bias and Dark Current Model Coefficients

	Bias Model Coefficients (Equations (2) and (3))							Active Region Dark Coefficients (Equation (4))	
Camera and S/N	a_0	a_1	a_2	Offset	b_0	b_1	b_2	c_0	c_1
MER-1 left; S/N 115	−9.55	6.97	0.0523	20	−13.85	42.21	0.0124	0.0134	0.0943
MER-1 right; S/N 114	−20.25	17.71	0.0223	20	−17.67	39.55	0.0120	0.0149	0.0927
MER-2 left; S/N 104	−2.59	0.764	0.201	20	8.23	27.83	0.0146	0.0180	0.0911
MER-2 right; S/N 103	−12.46	10.07	0.0353	20	−28.86	46.14	0.0106	0.0143	0.0967

and utilize the actual value of the video offset in the Pancam calibration pipeline (stored in the OFFSET_MODE_ID label field in MER PDS format data files).

[48] The bias level of the MER CCDs is determined from the (optionally downlinked) reference pixels. However, the values of the 32 reference pixels can vary because of two main effects. First, reference pixel values in the same image row can vary because of charge transfer effects from CCD structures near the right (downstream) side of the horizontal register, which can generate a slow rise in the bias level from reference pixels 17 to 30 (pixel 32 is set by the FPGA to the camera ID value, and 31 is set to be a copy of 30 because the timing of the pixel readout results in one missed pixel per 1056-pixel horizontal register row). The reference pixel 17 to 30 bias increase (Figure 14a) is temperature dependent but is not expected to be significant for most images acquired on Mars. The second source of potential reference pixel variations is a slow increase in the temperature of the MER camera electronics as the CCD is being read out. This effect manifests itself as a small increase in the bias level from the initial (first-read) reference pixel rows to the last rows read out of the array ~5.12 s later (Figure 14b). Over the entire range of temperatures and exposure times used during calibration, this trend was found to have the same shape and amplitude, and could be modeled with a function of the form

$$\mathrm{Bias}[R] = \mathrm{ref}_{\mathrm{mean}} + a_0 + a_1(R + \mathrm{offset})^{a_2}, \quad (2)$$

where $\mathrm{ref}_{\mathrm{mean}}$ is the mean value of the reference pixels across all rows, R is the row number, and offset is a term added to allow for a better fit at low row number where the curve is steeper (we used a value of offset = 20). An example of this function fit to Pancam data is shown in Figure 14b. In the Pancam preflight calibration data, the reference pixel information is always available, so we could calculate $\mathrm{ref}_{\mathrm{mean}}$ and fit the values of a_0, a_1, and a_2 from equation (2) directly for each image, and then use the resulting equation to remove the bias. We found that the coefficients a_0, a_1, and a_2 are different from camera to camera, but are independent of temperature for a given camera. For a given camera, we also found that $\mathrm{ref}_{\mathrm{mean}}$ is dependent primarily on the electronics temperature and video offset value, and that it varies from camera to camera, probably because of slight differences in the specific characteristics of individual resistors and capacitors in each camera's electronics.

[49] We did not need to develop a temperature-dependent model for the bias for the preflight calibration data because the reference pixels were always returned with those images. However, during operations on Mars, reference pixels will usually not be returned, in order to maximize downlink efficiency. Thus we derived a temperature-dependent model to determine a bias value in Pancam images if the reference pixels are not available. As mentioned earlier, the amplitude and shape of the increasing trend in the bias is independent of temperature and exposure length, so that we only need to determine the relationship between temperature and the mean bias value to properly model the bias level. After the effect of the video offset is removed, the bias is expected to have an exponential relationship with camera electronics temperature. There may also be a small secondary effect that is correlated with CCD temperature, but because CCD and electronics temperatures in all of our test data are very highly correlated, we were not able to separate these effects. As a result, we developed a model based solely on the electronics temperature and the video offset using the following relationship:

$$\mathrm{mean}_{\mathrm{bias}} = b_0 + b_1 \exp(b_2 T) - \Delta\mathrm{Bias}, \quad (3)$$

where T is the electronics temperature in °C and ΔBias is from equation (1). The bias coefficients for the four flight Pancams are summarized in Table 5, and graphical representations are shown in Figure 14c.

4.2.6. Dark Current

[50] Thermal noise induces electron liberation in most semiconductor detectors like the MER CCDs, producing a temperature-dependent current in the devices even in the absence of illumination. This dark current accumulates in both the active (imaging) and frame transfer regions of the CCD, but the rate of dark current accumulation is different between the two regions. The shielded region has a lower rate of dark current generation because of surface state passivation by hydrogen in the opaque metal mask that covers this part of the CCD. Component-level testing showed the MER CCD shielded regions to have a factor of 4–5 lower dark current generation rate than the active regions, and this result is consistent with our modeling of the dark current calibration data discussed below. The dark current accumulation rate was also found to vary from pixel to pixel within each region, because of intrinsic differences in pixel responsivity and effects related to the specific layout of the surface and buried photolithography structures on the MER CCDs. We have modeled the active and masked region dark current values separately in order to determine the total portion of the signal due to bias and dark current. For these models, we assumed that any dark current that accumulates during the ~5 ms initial frame flush or the ~5 ms frame transfer from the active region to the masked region of the CCD is incorporated into the masked region dark current calculation.

[51] To model the dark current, we used a set of dark images (no light source illuminating the CCD) taken at

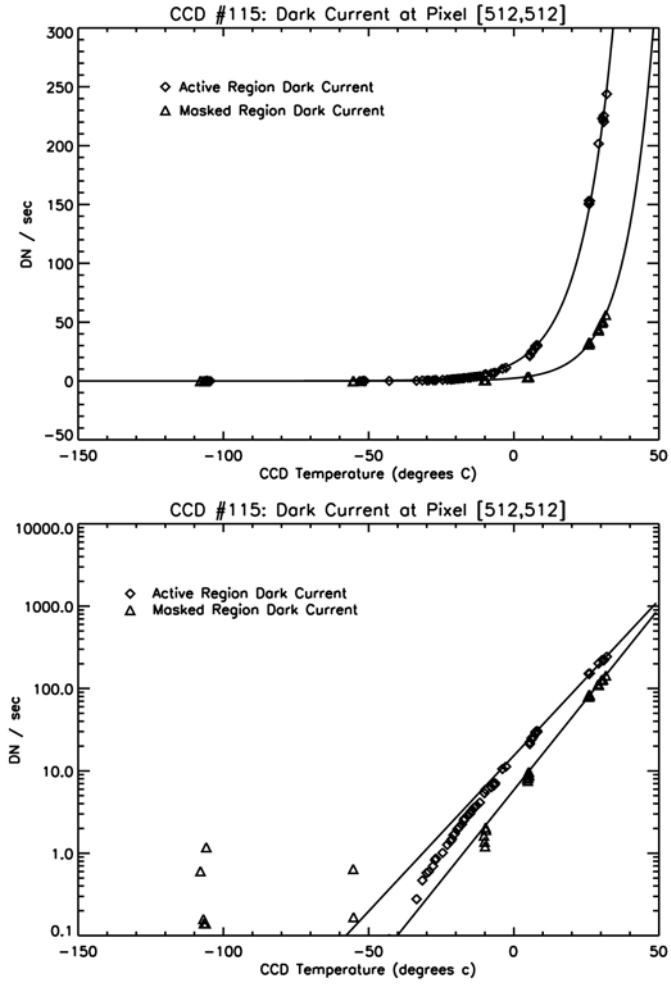

Figure 15. (top) Linear and (bottom) logarithmic plot of data and model for dark current DN/s generated for pixel (512, 512) during Pancam masked area readout (triangles) and during integration in the CCD active area (diamonds). The active area and masked region dark currents are modeled as exponential functions with parameters compiled in Table 5. Below about −20°C the models diverge from the (noisy) data because there is little or no dark current detectable in the cameras at these temperatures for typical exposure times expected on Mars. Data are from MER-1 (MER-B) Pancam serial number 115.

different temperatures and different exposure lengths, including a number of zero-length exposures. Our first step was to remove the bias level from the images, using equation (2) and data from the reference pixels associated with each calibration image. To get the most accurate value for the bias, we chose to use only pixels 4–16 from the reference pixels (Figure 14a) as the average values for these reference pixels were within a few tenths of a DN of each other.

[52] For all areas where dark current accumulates, we expect an exponential relationship between the rate of dark current accumulation and CCD temperature. Thus the total dark current DN accumulated over time t in ms and at a constant temperature T should be:

$$\text{dark current} = tc_0 \exp(c_1 * T). \quad (4)$$

Our next step was to model the dark current accumulation in the masked region of the CCD during frame readout. To model this, we used only zero-exposure dark images. By using zero-exposure images, there is no active area dark current accumulation, and so the resulting image value results only from the bias and dark current accumulation in the masked region. We removed the bias using equation (2), and were left with a set of images with DN values resulting solely from dark current accumulation in the masked region of the CCD during the fixed period of time corresponding to the frame readout.

[53] To characterize pixel-to-pixel variations in the dark current, we modeled each pixel separately in the images. Using our set of zero-exposure images (at different temperatures) with bias removed, we were able to use a least squares fitting algorithm to derive the c_0 and c_1 coefficients from equation (4) for most image pixels, along with error bars on the values of the coefficients. The fit for an example pixel is shown in Figure 15. However, as the row number decreased (corresponding to rows in the storage area closer to the horizontal readout register of the CCD), the total dark current became smaller and smaller, and the resulting DN values in those rows became dominated by noise, making the fitting error estimates very large. It was therefore nearly impossible to get a reliable fit to the exponential function to generate the dark current model coefficients in the first few

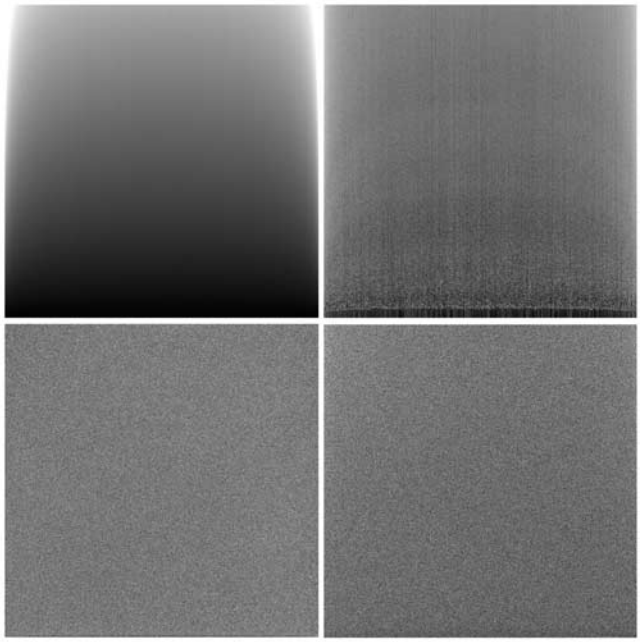

Figure 16. Image versions of the average Pancam dark model coefficients shown in Table 5. (top) Example Pancam dark current model images of flight camera number 115's masked region coefficients (left) c_0 (image stretch = 0.2–17.0) and (right) c_1 (image stretch = 0.098–0.108) from equation (4). (bottom) Example Pancam dark current model images of flight camera number 115's active region coefficients (left) c_0 (image stretch = 0.010–0.017) and (right) c_1 (image stretch = 0.093–0.096) from equation (4).

rows. Luckily, because the total dark current is so small there, even a poor fit to the coefficients does not produce a modeled value of dark current that is very far from the actual value in an absolute sense. We found that the dark current in the masked region is not flat across a given row, but is lowest at the center of the image, increases gradually toward the edges, and then tails up sharply near the edges. This pattern is mirrored in the c_0 coefficients and also more subtly in the c_1 coefficients (Figure 16). The sharp spikes in the first and last columns of every image are a manifestation of the fact that these columns often show a much higher level of dark current in MER CCD images, probably from thermal noise generated by amplifiers and other surface and buried photolithography structures adjacent to the edges of the CCD. The masked area dark current coefficients are stored in image form for each camera, and can be used to quickly generate a ''masked-region dark current image'' at a given temperature.

[54] Finally, after removing the bias and masked region dark current, we were able to process the nonzero-exposure dark calibration images to model the active region dark current. Again, to characterize pixel-to-pixel differences in the CCD, we chose to model the dark current in each pixel as a separate function. On the basis of inspection of a large number of images, to avoid effects from saturation or excessive dark current migration at high temperatures, we ignored pixels with dark current induced DN values greater than 3000. Equation (4) was used to fit the active area dark current data, and an example fit is shown in Figure 15. Most pixels that tended to saturate sooner (hot pixels) still showed the same exponential relationship with CCD temperature; they simply had higher c_0 coefficients. The active area dark current coefficients are stored in image form for each camera (Figure 16), and can be used to quickly generate an ''active region dark current image'' at a given temperature. Table 5 lists the coefficients for the average dark current of the active region of each CCD for the four flight Pancams. The Pancam dark model is continually being refined based on preflight system level rover test images. For example, the model is being updated to include dark current changes induced by ''self warming'' in the CCD and electronic boxes during long integrations and/or long periods of extended imaging. Details on the dark current model updates are reported by *Bell et al.* [2003b]. The dark model will be validated in flight by acquiring dark current images during cruise and on Mars by imaging through the solar ND filters to simulate dark conditions at Mars daytime temperatures. We anticipate needing to continue to refine the dark model during flight because of the known variations in dark current induced by radiation damage of CCD pixels during cruise and on the surface.

4.2.7. Filter Performance

[55] Different aspects of Pancam filter performance were assessed at the component and subsystem levels. Variations in the effective center wavelength and bandwidth were assessed as a function of temperature and angle of incidence by the filter vendor at the component level. All filters show a smooth increase in effective wavelength of 1.5 ± 0.5 nm as the temperature was transitioned from +25°C to −50°C, but there was no associated change in the bandwidths. This wavelength shift is consistent with expectations for thin film interference filters, and the magnitude of the shift with temperature is too small a fraction of the overall band pass to significantly impact scientific interpretations. The filters also show a decrease in effective wavelength of 1.5 ± 1.0 nm as the angle of incidence increases from 0° (on axis) to 9° (edge of field). Again, this is too small a change to result in a significant science impact. Filter out-of-band blocking performance was assessed both at the component and subsystem level via testing at JPL. The average rejection band level (defined as the integral of the filter's transmissivity in the region outside of the ±1% passband limits divided by the integral of the total transmissivity from 400 to 1100 nm) for the narrowband geology filters is 1.1 ± 0.7%, which was acceptably close to the requirement of 1%. The short-pass and long-pass geology filters exhibited larger rejection band levels (1.5–5.0%) but were still judged to be acceptable based on the smooth and monotonic nature of their out of band transmission. None of the geology filters have meaningful leaks outside of their nominal band passes.

[56] It was extremely difficult to characterize accurately the blocking performance of the solar filters because of the difficulty in imaging monochromatic sources through a neutral density 5 coating. However, component-level JPL and vendor data were obtained to try to characterize their performance. The short wavelength solar filter (L8; 440 nm) exhibits a red leak near 700 – 750 nm (Figure 6) that may contribute substantial red light to the blue solar filter's observed flux. Unfortunately, the test and characterization data required to accurately characterize this effect are sparse

and sometimes conflicting. Therefore the ultimate characterization of the magnitude and implications of this red leak will need to come from L8 imaging during operations on Mars. The long-wavelength solar filter (R8; 880 nm) does not appear to exhibit any meaningful leaks outside of its nominal band pass.

4.2.8. Temperature Dependence of System Spectral Throughput

[57] The spectral throughput of each flight Pancam geology filter was measured using a monochromator while the cameras were under near-vacuum and at three temperatures ($-55°C$, $-10°C$, and $+5°C$). Small variations in effective center wavelength were detected, consistent with those seen at the component level for the filters and the CCD. None of the variations were significant enough to impact scientific interpretations. The system level spectral throughput curves in Figure 6 show the representative shapes of the Pancam band passes at a temperature of $-10°C$.

4.2.9. Flatfields

[58] Images of pixel-to-pixel responsivity variations, or flatfields, were measured through each Pancam filter during standalone camera testing under ambient conditions and in near-vacuum at three temperatures ($-55°C$, $-10°C$, and $+5°C$). Each camera was pointed into an integrating sphere to acquire images of a field known to be spatially ''flat'' to within 1–2%. Spatial variations in responsivity in imaging systems like Pancam can arise from one of four sources: (1) intrinsic variations in the responsivity of pixels in the detector; (2) responsivity variations related to $\cos^4$ falloff with distance from the center of the optical axis (field angle); (3) contamination (e.g., dust and scratches) or fabrication nonuniformities of the optics and/or filters; and (4) undesired nonuniform radiance arising from scattered or stray light in the camera system and/or the test equipment (sphere, vacuum chamber window, etc.). An extensive parts screening exercise was conducted prior to assembly of the cameras in order to identify CCDs with minimal variations in intrinsic responsivity. This exercise produced a set of Pancam flight CCDs with remarkably uniform responsivity across the array and few (or no) ''bad'' pixels. The optics and filters were inspected by the vendors and JPL Quality Assurance personnel and found to either be free of, or have an acceptably low level of, scratches, digs, pinholes, or other manufacturing imperfections. Stray and scattered light within Pancam was also found to be at too low a level to generate noticeable flatfield variations (see section 4.2.11.4 below). Some images were found to contain high-spatial-frequency artifacts related to imperfections in the integrating sphere internal coating or reflections off the vacuum chamber window.

[59] The flatfield response through all Pancam filters is dominated by low spatial frequency components like the $\cos^4$ falloff (Figure 17), which can produce decreases in responsivity of 5–10% along the edges and in the corners of the field of view. High-spatial-frequency responsivity variations with amplitudes of 1% or less have been detected in ground calibration measurements (e.g., a 32-row ''step-and-repeat'' pattern intrinsic to the surface and/or buried photomasks used in CCD fabrication; Figure 17), but these effects are not noticeable in normal images. The final Pancam preflight flatfield calibration images are normalized to a mean of 1.0. We also generated ''flatfield uncertainty images'' from the 30 to 50 sequential images used for determination of the system radiometric stability (see section 4.2.10.4 below). The average value of these uncertainty images is never larger than 0.013, and is typically more like 0.005. We will propagate this small source of additional uncertainty formally through the calibration pipeline.

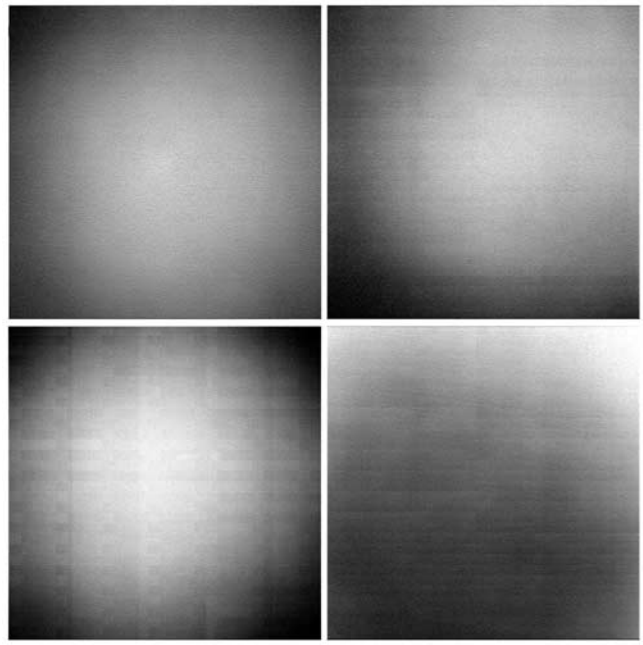

Figure 17. Representative Pancam flatfield images. (top left) Pancam serial number 104 L1 flatfield. This is the empty filter slot and so the variations here are from variations in the CCD and optics alone. The variations are shown here contrast enhanced to the ±5% level (2σ). (top right) Pancam S/N 103 R2 (754 nm) flatfield image, contrast enhanced to the ±5% level (2σ). (bottom left) Pancam S/N 104 L7 (440 nm) flatfield. The regular ''brick-wall-like'' patterns are a manifestation of surface and buried photomask structures in the CCD. This image is heavily contrast enhanced, however, and these variations are detectable only at the $\leq$1% level. (bottom right) Pancam S/N 103 R7 (1001 nm) flatfield. Similar CCD mask structures can be seen in this flatfield image, but their contrast is at the $\ll$1% level. The latter two flatfield artifacts should not be detectable in normal Pancam imaging on Mars.

4.2.10. Absolute Responsivity

[60] The responsivity of each Pancam through each geology filter was determined at the standalone camera level in near-vacuum at three temperatures ($-55°C$, $-10°C$, and $+5°C$). The responsivity of the solar filters was also determined at these three temperatures for the MER-1 (''Opportunity'') Pancams (S/N 114 and 115), but was only determined at $+5°C$ and $-10°C$ for the MER-2 (''Spirit'') Pancams (S/N 103 and 104). Each camera obtained multiple images of the entrance aperture of an integrating sphere using the geology filters. The sphere itself was calibrated with a NIST-traceable diode radiometer. Diode output voltages were recorded along with each image. The absolute calibration accuracy of the diode was measured before and after the camera calibration measurements by the JPL Standards Laboratory, and is estimated to be 1.5 ± 0.1% over the Pancam band-pass range. Each

Table 6. Pancam Initial Preflight Radiometric Calibration Coefficients

Camera and S/N	Filter Name	$R(T)$,[a] (W/m^2/nm/sr)/(DN/s)	NESR (Typical Soil), W/m^2/nm/sr	Default Video Offset
S/N 115; left Pancam, MER-1, MER-B, "Opportunity"	L1	3.330E-07 − 1.029E-11 T	1.182E-04	4082
	L2	4.750E-06 + 3.607E-09 T	4.996E-05	4082
	L3	8.611E-06 + 1.345E-08 T	7.719E-05	4082
	L4	9.891E-06 + 1.803E-08 T	6.093E-05	4082
	L5	1.588E-05 + 3.288E-08 T	4.028E-05	4082
	L6	1.813E-05 + 4.290E-08 T	2.673E-05	4082
	L7	5.065E-05 + 1.717E-07 T	1.031E-05	4082
	L8	7.33 + 7.04E-03 T		4082
S/N 114; right Pancam, MER-1, MER-B, "Opportunity"	R1	4.198E-05 + 1.167E-07 T	1.213E-05	4071
	R2	4.607E-06 + 1.920E-09 T	5.123E-05	4071
	R3	6.023E-06 − 2.704E-09 T	8.077E-05	4071
	R4	8.454E-06 − 1.474E-08 T	6.714E-05	4071
	R5	5.766E-06 − 1.646E-08 T	6.511E-05	4071
	R6	7.607E-06 − 3.036E-08 T	6.551E-05	4071
	R7	1.009E-05 − 1.067E-07 T	6.864E-05	4071
	R8	0.405 − 8.59E-04 T		4071
S/N 104; left Pancam, MER-2, MER-A, "Spirit"	L1	3.174E-07 − 2.111E-11 T	5.271E-05	4095
	L2	4.470E-06 + 2.241E-09 T	4.627E-05	4095
	L3	8.123E-06 + 1.041E-08 T	3.968E-05	4095
	L4	9.792E-06 + 1.669E-08 T	2.960E-05	4095
	L5	1.504E-05 + 2.814E-08 T	2.236E-05	4095
	L6	1.751E-05 + 4.282E-08 T	1.394E-05	4095
	L7	4.253E-05 + 1.293E-07 T	1.146E-05	4095
	L8	7.14 + 5.64E-03 T		4095
S/N 103; right Pancam, MER-2, MER-A, "Spirit"	R1	5.040E-05 + 3.039E-07 T	9.543E-06	4066
	R2	4.427E-06 + 2.596E-09 T	4.784E-05	4066
	R3	5.489E-06 − 1.707E-09 T	6.142E-05	4066
	R4	8.537E-06 − 1.462E-08 T	5.973E-05	4066
	R5	5.798E-06 − 1.575E-08 T	5.022E-05	4066
	R6	7.633E-06 − 2.871E-08 T	4.543E-05	4066
	R7	9.292E-06 − 7.973E-08 T	4.613E-05	4066
	R8	0.5049 − 9.29E-04 T		4066

[a] T is in °C.

camera also obtained multiple images of the filament of a 250 W calibrated tungsten lamp through each of its solar filters at all three temperatures. Earlier measurements of the transmissivity of the vacuum chamber window were used to remove its spectral effects from the images. Representative responsivity coefficients at −10°C as well as the slope and offset of a linear function describing responsivity variations with temperature for all filters in all four flight Pancams are summarized in Table 6.

4.2.10.1. Geology Filters

[61] Images of the integrating sphere were calibrated to remove the effects of bias, dark current, frame transfer smear, vacuum chamber window transmission, and flatfield variations. Multiple such "calibrated DN" images were obtained for each combination of filter and environmental conditions, and a mean image (DN/s) was calculated. The average value of this mean image was then compared to the radiance measured by the integrating sphere's diode radiometer to produce a mean responsivity coefficient, and then this process was repeated for other filters to generate the coefficients listed in Table 6. The uncertainty on the responsivity coefficients was conservatively estimated from the standard deviation the mean image for each filter, which is dominated by small variations in flatfield response and which is large compared to the uncertainty on the absolute calibration of the diode radiometer. Analysis of the temperature dependence of the responsivity of the geology filters was found to be consistent with the slope of the CCDs temperature-dependent QE variations near the filters' effective wavelengths (Figure 12). The responsivity coefficients vary linearly with temperature, with the slope and offset values for each camera/filter given in Table 6.

4.2.10.2. Solar Filters

[62] Images of the tungsten lamp were calibrated to remove the effects of bias, dark current, and frame transfer smear variations and were analyzed, using a similar process as for the geology filters, to generate the coefficients listed in Table 6. The temperature dependence of the solar filter responsivity was assessed by performing the analysis on data acquired at two or three temperatures over Pancam's nominal operating range. The slope of the temperature variations was found to be consistent with the slope of the CCDs temperature-dependent QE variations near the effective wavelengths of the solar filters (e.g., Figure 12). Because it was not possible to illuminate the full FOV with a uniform source bright enough to generate significant signal through the solar filters, we instead attempted to test for spatial variations in solar filter responsivity across the field by acquiring lamp filament images at five or more different field positions (center, upper left, lower left, etc.). Only one of the four flight Pancams (S/N 114, the MER-1 Opportunity rover's right camera, carrying a 880 nm solar ND filter) showed any repeatable spatial variability, with a responsivity increase in the center and upper right quadrants of the image suggesting the possible presence of a mild scratch or pinhole in the filter. Operationally this should have no impact on this solar filters' science or navigation tasks if the ~22 pixel wide image of the Sun is kept away from the center of the image and out of the upper right quadrant.

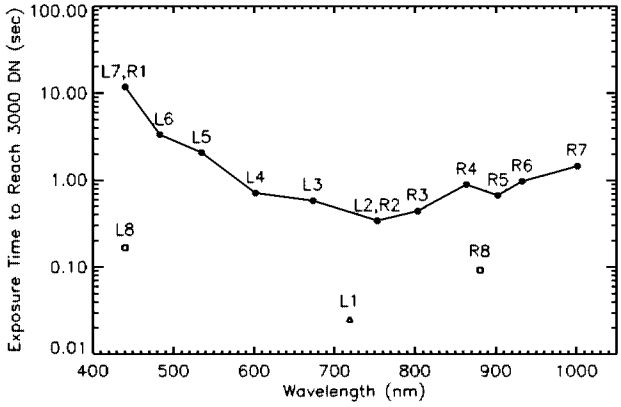

Figure 18. Predicted exposure times for Pancam filters to reach 3000 DN on Mars, assuming imaging of typical bright soils (for the geology filters) or the Sun at zenith (through the solar filters) through a clear atmosphere at −10°C.

4.2.10.3. Independent Validation

[63] We obtained images of an engineering model Pancam calibration target illuminated by a NIST calibrated tungsten lamp from a known distance and geometry to provide an independent validation of our geology filter radiometric calibration coefficients determined using the integrating sphere/diode setup described above. The coefficients in Table 6 and the calibration target BRDF model described below were used to predict the DN level of the calibration target white, gray, and black rings for a given exposure time. We found that our predictions were within the actual measured DN to within 5–10% for all filters. As this was within the measurement and setup uncertainties of our test, we regard this as an adequate validation of the coefficients in Table 6.

4.2.10.4. NESR

[64] Noise in remote sensing systems can be expressed in terms of the equivalent amount of power in a hypothetical "noise signal," also known as the Noise Equivalent Spectral Radiance (NESR; [e.g., *Baker et al.*, 1975; *Izenberg et al.*, 2000]). Combining estimates of an instrument's spectral and temperature-dependent NESR values with the expected radiance from the target provides a way to assess the signal to noise ratio (SNR) of the measurements. Since NESR is a statistical parameter, determining its value for a particular instrument under particular operating conditions requires a statistically significant number of repeated measurements. We obtained such measurements by obtaining 30 to 50 sequential images of a stable integrating sphere aperture with each flight camera and filter combination in near-vacuum at three temperatures (−55°C, −10°C, and +5°C) and at three different sphere radiance levels, corresponding to the nominal radiance expected on Mars from typical bright soils, typical dark rocks, and the sky. This enormous data set was calibrated to remove the effects of bias, dark current, and frame transfer smear, and it is the same data used to derive the flatfield images and absolute responsivity coefficients described above. The standard deviation was calculated for each pixel in each stack of 30 to 50 images, and the mean of this standard deviation image was multiplied by the appropriate responsivity coefficient to generate estimated NESR values in $W/m^2/nm/sr$ for each filter/temperature/incident radiance combination. NESR values for imaging of a radiance source like that expected from typical bright soils on Mars [*Huck et al.*, 1977; *Maki et al.*, 1999] at −10°C are listed in Table 6. These values predict instrumental SNR values ranging from about 250 to 700 for the Pancam geology filters. Pragmatically, though, instrument SNR values are always limited to being below about 350 to 400 because of the gain and full well capacity of the Pancam CCD. And realistically, other sources of systematic noise (uncertainties in absolute calibration, flatfielding, dark current modeling, compression, etc.) will act to yield actual SNR values that are lower than this, but which are still expected to be greater than ~200, on average, for most images acquired through the geology filters.

4.2.10.5. Predicted Exposure Times on Mars

[65] The responsivity coefficients in Table 6 plus previous measurements of typical Mars surface irradiances from the Viking Landers [*Huck et al.*, 1977] and Mars Pathfinder [*Maki et al.*, 1999] are used to generate estimates of the expected exposure times required for the Pancam filters on Mars. Figure 18 shows a summary of the expected exposure times required to obtain a signal level of 3000 DN in each filter, assuming imaging of typical bright soils (for the geology filters) or the Sun at zenith through a clear atmosphere (for the solar filters). Atmospheric dust or solar zenith angle increases will act to increase these exposure times in the same way as described by *Smith et al.* [1997a] for the Mars Pathfinder IMP camera.

4.2.11. Image Quality

[66] Image quality parameters for the four flight Pancams were determined at room temperature and ambient pressure, and spot check validated during thermal vacuum testing of each flight rover. System characteristics that were determined include image contrast as a proxy for best focus determination, Modulation Transfer Function (MTF), focal length, working *f*/#, FOV, IFOV, and scattered/stray light intensity.

4.2.11.1. Focal Length, *f*/#, IFOV, and FOV

[67] Pancam's geometric properties were characterized from images of a grid calibration target consisting of an array of white circular dots painted on a background of black anodized aluminum. Each dot is 12.497 ± 0.025 mm in diameter and the dots are spaced 41.478 ± 0.025 mm apart. Determination of the centroid positions of the dots in Pancam images at two distances, combined with the lensmaker's formula, allowed derivation of the geometric parameters which are summarized in Table 7. As expected, there is no observed wavelength dependence of these geometric properties for the Pancams.

4.2.11.2. Focus

[68] The horizontal and vertical contrast of alternating white and black bars on a specially designed "bar target" (Figure 19a) was used to confirm that the flight Pancams are performing as designed in terms of focus. Contrast here was defined as the difference between the average white and

Table 7. Pancam Geometric Parameters

Camera, S/N	Focal Length, mm	FOV, deg	IFOV, mrad/pixel	*f*/#
103	43.018 ± 0.220	16.052 ± 0.082	0.2736 ± 0.0014	20.00 ± 0.06
104	43.165 ± 0.220	15.978 ± 0.099	0.2723 ± 0.0017	20.06 ± 0.09
114	43.065 ± 0.220	16.015 ± 0.068	0.2730 ± 0.0012	20.02 ± 0.06
115	43.019 ± 0.220	16.032 ± 0.094	0.2733 ± 0.0016	20.00 ± 0.03

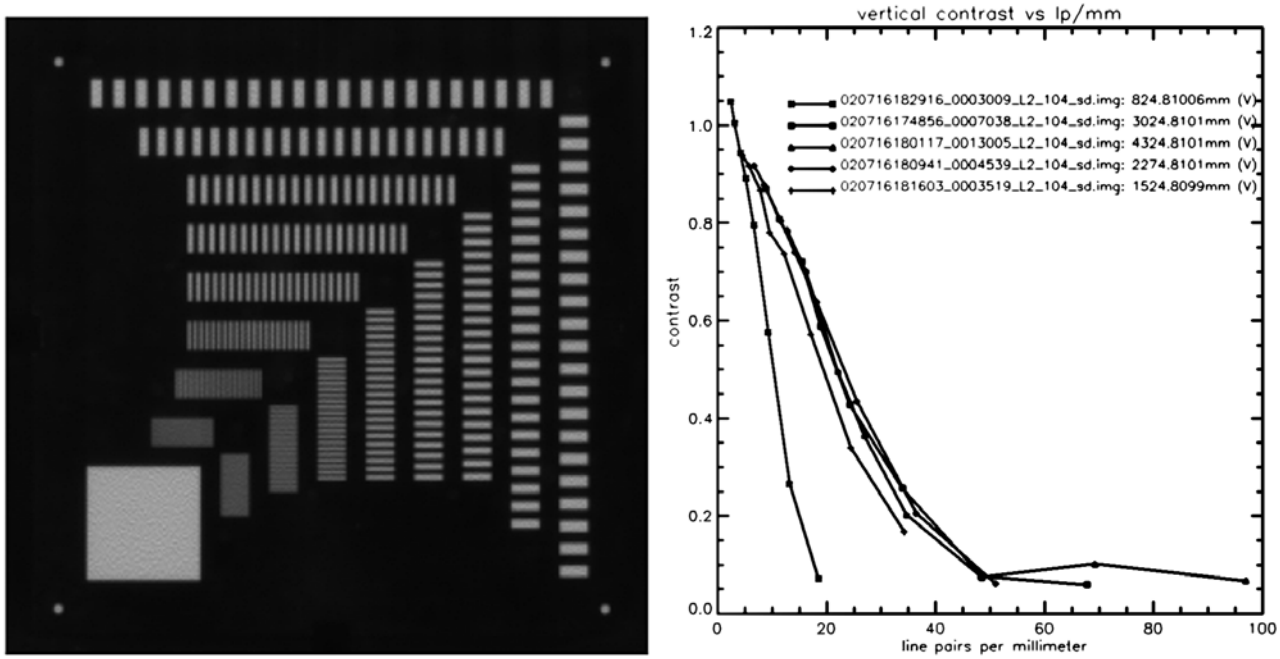

Figure 19. (left) Pancam image of etched bar target used for focus and MTF characterization measurements. The largest bar patterns have a spatial frequency of 1.04 mm/line pair and the smallest (unresolved in this image) are at 7.90 mm/line pair. (right) Example Pancam vertical contrast results for bar target images at five distances ranging from 0.82 (leftmost curve) to 4.32 m (rightmost curve).

black pixel values (over a particular region of interest) divided by the total white plus black pixel level above the background. An example calculation for five distances from the bar target to Pancam is shown in Figure 19b. The results validate the design and show that Pancam is in best focus from 3 m distance and (indistinguishably) beyond, that it is still well focused near 1.5 m, and that the focus degrades gracefully at shorter ranges. Contrast values decrease with increasing wavelength, at a level consistent with expectations based on the λ/D nature of diffraction in optics. The contrast results are statistically the same between the two left and two right flight Pancams, indicating no measurable differences in focus among the cameras. The contrast data, along with MTF results presented below, show that the best Pancam image quality is actually obtained through the polychromatic L1 (''empty'') filter position.

4.2.11.3. MTF

[69] The Modulation Transfer Function (MTF) is a standard measure of image system performance for precision optical equipment [e.g., *Sitter et al.*, 1995]. The MTF is defined as the magnitude of the Fourier transform of the optical system response to an input impulse. The calculation of MTF for a sampled system like an array of CCD detector pixels is determined through the measurement of the reduction in amplitude of the fundamental frequency component of an input impulse obtained from imaging targets like our bar target (Figure 19). However, the discrete sampling of the system causes the property of spatial invariance to be lost, and overlapping can occur in the high spatial frequencies of the input impulse. This overlapping is known as aliasing and if not considered appropriately it can cause incorrect estimates in the amplitude of the MTF. Our bar pattern frequencies were chosen so as to minimize such aliasing effects [*Sitter et al.*, 1995].

[70] Pancam MTF values were found to be consistent with, though somewhat below, the ideal detector MTF values for such an optical system using equations like those in *Holst* [1998]. MTF, like contrast, peaks near 3 m distance for Pancam and reveals a depth of field that surpasses the largest bar target distance measured (4.3 m). MTF was also observed to decrease linearly with wavelength, as expected, among the different Pancam narrowband filters.

4.2.11.4. Scattered and Stray Light

[71] Internal scattered light from on-axis sources and external stray/scattered light from off-axis sources were characterized using a bright (effective signal level $> 2 \times 10^6$ DN) fiber optic light source illuminating the camera over a variety of field angles and intensities for the geology filters, or by obtaining ultralong (335 s) field-filling integrations using an integrating sphere as the illumination source for the solar filters. Weak reflections and other ghost image artifacts were seen in all the geology filter images, and their positions varied repeatably and systematically with changes in fiber illumination position. Signal levels of ghost images were typically 10^{-5} to 10^{-6} of the illumination level. Such artifacts are not expected to be detectable in nominal imaging data on Mars.

[72] Simulations of a bright (solar-like) source just outside of the Pancam field of view (within $\sim 1^\circ$) reveals similarly weak ghost images, validating the expected performance of the optics baffles. Consequently, and if the PMA pointing is as reliable and repeatable on Mars as it was during preflight tests, Pancam sky imaging with the geology filters at angles very close to the Sun should be possible, enabling science observations with the greatest sensitivity to atmospheric aerosol physical properties. Weak ghost images and pinhole-like reflections were also detected in the solar filters after long exposures, but they are

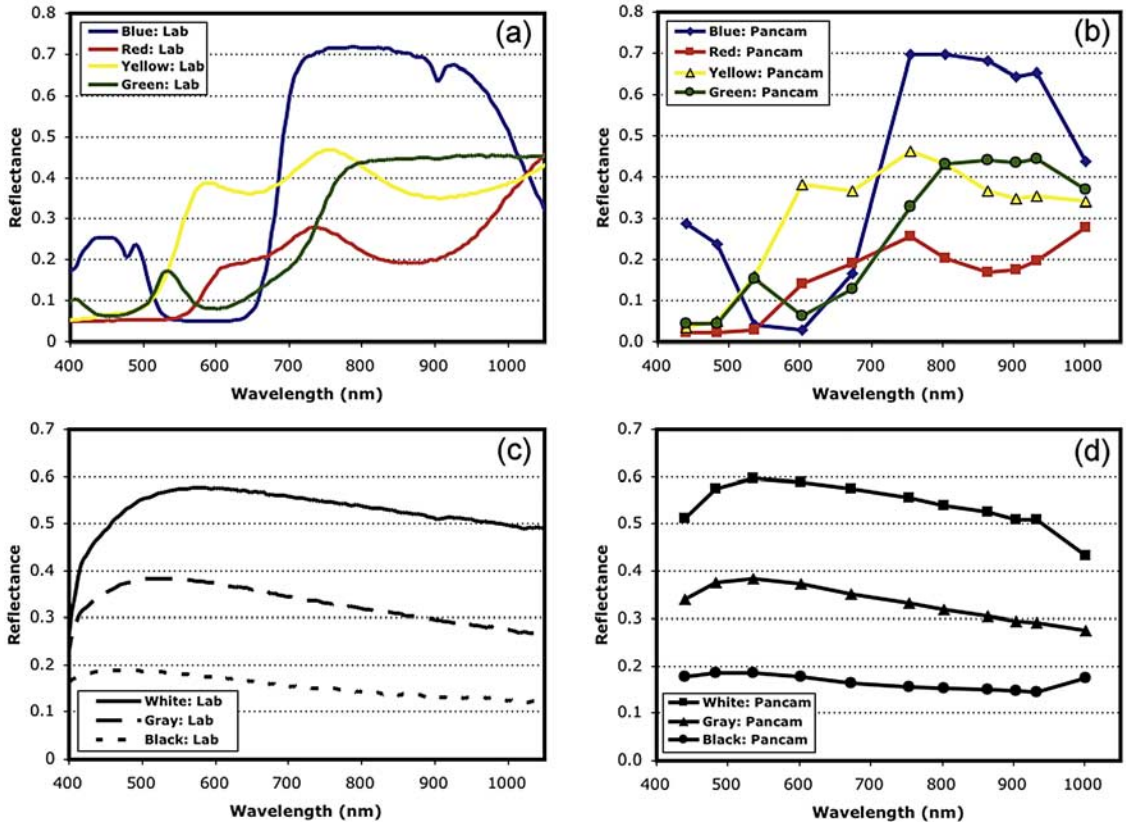

Figure 20. Comparison of laboratory-measured directional hemispheric reflectance spectra of the Pancam calibration target reflectance materials versus relative reflectances as determined by calibrated Pancam flight camera S/N 103 and 104 measurements made during MER-2 (MER-A) rover thermal vacuum calibration activities. (a) Lab spectra of cal target corner color chips. (b) Pancam spectra of cal target corner color chips. (c) Lab spectra of cal target grayscale rings. (d) Pancam spectra of cal target grayscale rings. Small remaining differences between the laboratory data and Pancam measurements are due to residual uncorrected differences in illumination and viewing geometries between the measurements and, for the 1000 nm band (filter R7), to uncorrected effects related to the higher transparency of the RTV silicone calibration target materials at these long wavelengths. All of these effects will be incorporated in the calibration target model to be used during Mars surface operations.

repeatable and at an intensity level of <0.1% of the expected solar disk intensity. A combination of their low intrinsic intensity and operational approaches to keep the solar disk away from certain zones in the images (see above) imply that these effects are not expected to impact Sun imaging for science or navigation purposes.

4.2.11.5. Distortion

[73] Distortion was corrected in the Cooke triplet lens design of Pancam. We searched for evidence of distortion at the edges and corners of the field using images of the grid target described above. The lens was found to have residuals of less than 0.01% across the field. Essentially, no measurable distortion could be detected in Pancam images of the grid target, and none is expected in images from Mars.

4.2.12. EMI/EMC

[74] Electromagnetic Interference and Electromagnetic Compatibility (EMI/EMC) tests were performed using an engineering model Pancam at the standalone camera level to search for evidence of noise interference or electromagnetic susceptibility to frequencies like those transmitted and received by the rovers' high gain, low gain, and UHF antennae. No obvious signs of induced image noise were found above the random noise level (3–5% in these ambient temperature images). Testing at the rover system level showed that (1) the X-band receiver does not experience any interference from other rover operations, including imaging; (2) the UHF receiver does experience some interference/signal degradation when the Pancam is operating; and (3) none of the MER cameras are susceptible in terms of noise or image contamination from other rover operations, including X-band and UHF. On the basis of these test results, a flight rule has been adopted to prevent operation of the Pancams and other MER science instruments during UHF communications passes. No such restrictions exists for X-band (high-gain antenna) communication passes, however.

4.2.13. Pancam Calibration Target Characterization

[75] The reflectances and photometric properties of the Pancam calibration target standard materials (white, gray, and black rings and the corner color chips) have been characterized at the component level using representative samples of the material, at the standalone target level using an engineering model (EM) of the target, and at the system level using the flight targets mounted on the rovers.

[76] Reflectances of the calibration target samples were measured from 348 to 1200 nm at 4 nm spectral sampling using a Cary-14 directional-hemispheric spectrometer [e.g., *Morris et al.*, 1985, 2000]. Examples of these laboratory spectra are shown in Figure 20. We also obtained images of the flight calibration target during rover system thermal vacuum tests using each of the four flight Pancams. The Pancam data were calibrated for instrumental effects (bias, dark, frame transfer smear) and converted to relative reflectance (R* [*Reid et al.*, 1999]) using laboratory observations of the gray ring as the reference. Preliminary versions of the resulting 11-color Pancam "spectra" are also shown in Figure 20. The overall reflectance levels and spectral shapes between the Pancam and lab data are similar, and allow the major color, spectral slope, and solid state spectral absorption features between the samples to be distinguished. Ongoing refinements of the Pancam data reduction and calibration pipeline are expected to yield a better match to the laboratory data in filters where the differences are still unacceptably large. For example, the relatively large discrepancy between the Pancam and laboratory measurements for the 1000 nm band (filter R7) are known to be due to the higher transparency of the silicone rubber calibration target materials at these long wavelengths, allowing the reflectance "signature" of the underlying aluminum substrate to exert an influence on the detected signal. These and other viewing geometry effects are the subject of continuing analysis.

[77] In order to make accurate use of the Pancam calibration target images it is necessary to be able to predict the expected calibration target radiances for a given lighting geometry and wavelength. Therefore we have developed a Bidirectional Reflectance Distribution Function (BRDF) model for each of the seven reference areas on the target (white, gray, black, blue, red, yellow, and green). The model is based on BRDF measurements of reference areas at incidence and emission angles consistent with those expected during operations on Mars using the Bloomsburg University Goniometer (BUG) facility described by *Shepard* [2001] and the French Centre Nationale de la Recherche Scientifique (CNRS) facility described by *Pinet et al.* [2000].

[78] BUG data were obtained on sample pieces of reference material, and CNRS data were obtained on a fully assembled EM target. Both sets of measurements were acquired through a set of flight spare Pancam filters. The BUG sample measurements were measured at a fixed emission angle of 53.5°, which is approximately the angle that the Pancams will be viewing the target on the rover's -X solar panel, and were obtained at 169 separate incident-azimuth-elevation values. The observation points were chosen to provide overall uniform coverage of the scattering hemisphere, and dense coverage near opposition and specular reflection directions (Figure 21a). The light source was a 100 W quartz-tungsten halogen bulb which is filtered, chopped, and channeled along a fiber optic cable to an optical collimator at the end of a ~0.6 m long incidence arm. Relative uncertainties in these BRDF measurements are ~2%, and absolute uncertainties are ~10%.

[79] The CNRS data were acquired at a fixed emission angle near 65° and over a range of incidence angles from approximately 0° to 50° in 10° steps in the principle scattering plane as well as at a small number (six) of regularly spaced azimuth angles that are not in the principle plane. The light source for those measurements was sunlight, directed into the laboratory using a heliostat. Comparison between the CNRS and BUG Lab data provided validation of both sets of measurements. In addition, due to more natural incident light the effective wavelength of the system response of the CNRS system is much closer to the one expected for the Pancams on Mars. The CNRS data thus allow a better estimate of the error introduced into the BRDF by differing effective wavelengths between the system throughput of the BUG with Pancam filters inserted, versus the system throughputs of the Pancams themselves under Martian lighting conditions. This error was found to be less than 5%.

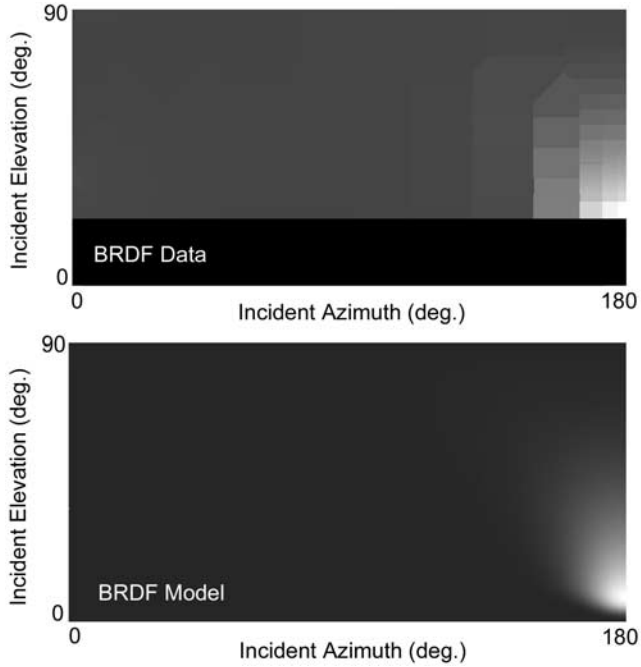

Figure 21. (top) Pancam calibration target BRDF data from the gray ring material at 750 nm and (bottom) the combined He-Torrence/Hapke model representation of the data. Black corresponds to a radiance factor of 0.0; white corresponds to a radiance factor of 0.5.

[80] The BRDF is defined as the ratio of the radiance of an arbitrary surface to the radiance of an ideal white Lambertian surface illuminated and viewed in an identical fashion. Mathematically,

$$\rho_{bd}(\theta_r, \phi_r, \theta_i, \phi_i, \lambda) = dI_r/dE_i, \quad (5)$$

where dI_r is the reflected radiance or intensity, measured in W/m^2/sr, dE_i is the incident energy flux, measured in W/m^2, θ_i and ϕ_i are the incident elevation and azimuth in degrees, θ_r and ϕ_r are the reflected elevation and azimuth in degrees, and λ is the wavelength. A mathematical model was developed to match the BRDF of the calibration materials. This model validates the laboratory measurements, allows more accurate interpolation between measured points along both the wavelength and azimuth-elevation axes, and could be useful for researchers attempting to model the expected effect of dust buildup on the calibration target [e.g., *Johnson et al.*, 2003].

[81] The calibration target reflectance materials are made from pigmented silicone RTV, a non-natural material with

photometric properties that are more amenable to modeling by computer science approaches, rather than by photometric models used for astronomical or geologic study of natural (rock, powder) surfaces. We found the model of *He et al.* [1991] to be quite effective (hereinafter referred to as the He-Torrance model). He-Torrance is a theoretical model based on physical optics. It describes the BRDF of a surface based on two surface roughness parameters (root mean square roughness, σ, and the autocorrelation length, τ) and the surface refractive index (n). The He-Torrence model produced a generally good fit to the calibration target materials measurements, but it was unable to account for the $\sim$10% backscatter lobe (Figure 21a).

[82] We believe that this backscatter is caused by a shadow hiding/light hiding effect, conceptually similar to the shadow hiding process described for natural powdered surfaces by *Hapke* [1986]. In this case, as the light source drops below opposition, more shadows become visible and the BRDF falls off. However, as the light source rises above opposition, rather than shadows becoming visible, directly illuminated regions become hidden. We modeled the backscattering component of the BRDF using a combination of the *Hapke* [1986] backscattering equation and the He-Torrence model (equation (6) below). While tests showed that the backscatter lobe is only moderately well fit by the Hapke model, we found that Hapke's representation did a better job than other astronomical coherent backscatter models that we examined. This approach adds another two parameters to the fit:

$$\rho_{bd} = P_{\text{he-torrance}}(\sigma, \tau, n)^* \left[1 + B_{\text{hapke}}(B_0, h)\right], \qquad (6)$$

where σ, τ, and n are the He-Torrence model parameters and B_0 and h are the opposition surge amplitude and width of the *Hapke* [1986] backscattering phase function parameter. This modified model was fit via a least squares hill climbing algorithm to photometric data from each calibration target region at each wavelength. An example model result for the gray ring in filters L2 and R2 (750 nm) is shown in Figure 21b. The resulting fits have an average error of 1%, and a maximum error of about 6% when compared against BUG and CNRS lab measurements.

[83] We also obtained a limited number of measurements designed to search for polarization sensitivity in the BRDF model. Several samples were measured using a polarizing filter in both parallel and perpendicular orientation. Most of the specular bulge appears to be composed of light polarized parallel to the surface of the calibration target, suggesting that operationally we should take care to consider this effect if obtaining calibration target images on Mars in a specular viewing geometry.

4.2.14. Pointing and Alignment

[84] The Pancams are mounted on a camera bar atop the PMA along with the Navcams (Figure 10). Alignment of these camera pairs was performed at ambient temperature using images of geometric test targets. Shims were used to set the toe-in angle and rotational and elevation coalignment to meet the requirements listed in Table 2. Once the camera bar was mounted to the PMA, additional images at the system level were obtained for geometrically surveyed test targets and rover fiducial points at a wide range of azimuth and elevation levels at ambient temperature and pressure in the high bay facility where the rovers were assembled. These imaging data were used to determine the true rotational limits of the PMA, including the angular positions of the azimuth and elevation hard stops, and to verify that the PMA met the Pancam pointing placement and pointing knowledge requirements listed in Table 2. The coalignment characteristics of the Pancams, Navcams, and the Mini-TES were assessed by acquiring images and spectra of special L-shaped heated targets designed to be straightforward for centroiding in both visible wavelength camera images and IR spectra. These targets were imaged at both ambient and thermal vacuum conditions. Other geometric targets, including a special "barber pole" target, were also imaged in ambient and thermal vacuum conditions to assess the Pancam to Hazcam coalignment parameters as well as to generate and validate detailed geometric camera models for each of the MER imagers. Additional discussion on the geometric camera models can be found in the work of *Maki et al.* [2003].

Figure 22. Pancam color composite image of rock target imaged during standalone camera thermal vacuum testing at -55°C. This is a rotated subframe of a full 1024 $\times$ 1024 image and was obtained using the MER-1 left Pancam (S/N 115). Pancam bands L4 (602 nm), L5 (535 nm), and L6 (483 nm) were used to generate an RGB composite simulating true color. The target was $\sim$2.3 m from the camera.

4.2.15. Rock/Standard Imaging Validation

[85] As a final validation of Pancam image quality, spectral responsivity, and as a way to generate data products useful for end-to-end Pancam data reduction pipeline testing, we obtained images of several specially designed rock and calibration standard targets during standalone camera and rover system thermal vacuum testing. The targets consisted of an array of small "tiles" that were fabricated by sawing and polishing naturally occurring rock and mineral samples (e.g., silicates, oxides, and carbonates) Some of the geologic samples have diagnostic spectral features that test Pancam's spectral detectability limits and

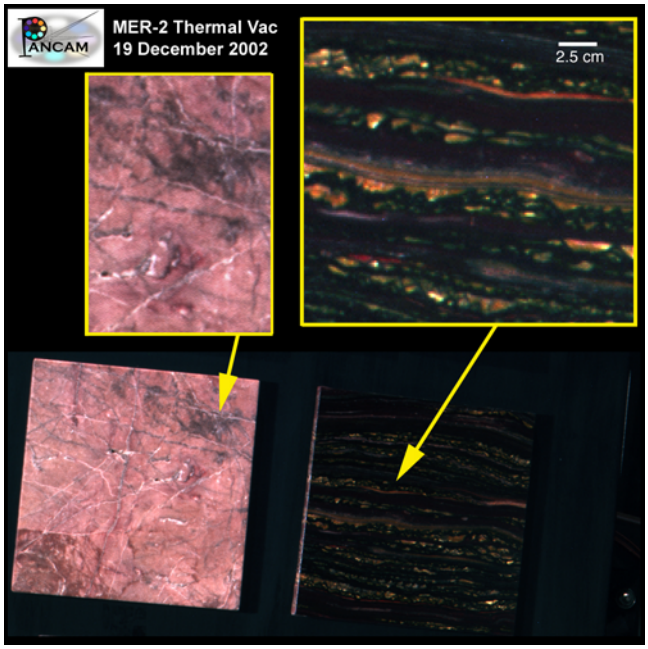

Figure 23. Pancam color composite image of rock target imaged during rover system thermal vacuum testing at −30°C. This is a montage from a full 1024 × 1024 image and was obtained using the MER-2 left Pancam (S/N 104). Pancam bands L4 (602 nm), L5 (535 nm), and L6 (483 nm) were used to generate an RGB composite simulating true color. The insets show fine-scale color and morphologic detail visible in the samples. The target was ∼2.5 m from the camera.

others contain fine-scale spatial detail that test Pancam's spatial resolution limits.

[86] Many tiles are representative of the geologic materials that are either known to occur or could reasonably be expected to occur on Mars. Some tiles are reflectance and color standards with a calibration traceable to NIST. An example Pancam color composite image of the rock target used during standalone camera calibration is shown in Figure 22, and an example Pancam color composite image of the rock target used during rover system thermal vacuum testing is shown in Figure 23. The former target was also imaged by the MER Navcam and Hazcam cameras [*Maki et al.*, 2003] and the latter target was also "imaged" by the MER Mini-TES spectrometer [*Christensen et al.*, 2003]. Similar tiles were individually imaged by the MER Microscopic Imager [*Herkenhoff et al.*, 2003] and individually analyzed by the MER Mössbauer spectrometer [*Klingelhoefer et al.*, 2003] and MER APXS. In addition, all the geologic samples are well characterized by a variety of standard laboratory compositional and mineralogic techniques, providing a cross calibration data set among all of MERs synergistic science instruments [e.g., *Morris and Graff*, 2002].

5. Mission Operations and Data Products

5.1. Operational Considerations

[87] Pancam is a very versatile instrument, and it will be used in a number of different ways during operations. A summary of the mission support objectives of the Pancam investigation is provided in Table 1. One of the most important operational roles will be to acquire full 360° panoramas. One of these per rover, in RGB color (L2: 753 nm, L5: 535 nm, and L6: 483 nm) and stereo (R2: 754 nm), is called for by the formal MER Level 1 Mission Success requirements (Table 2). We plan to meet this requirement while each rover is still on the lander preparing for egress. The approach for such a panorama will be to acquire red filter images at full resolution in both eyes, along with green and blue filter images at reduced resolution (using compression and/or downsampling) in the left eye. Such a panorama provides morphologic and textural information at the highest possible resolution, "true color" information at somewhat lower resolution, and good stereo ranging of the full scene around the rover. After this early "Mission Success" panorama, we plan to acquire full 360° Pancam panoramas rather infrequently because they take considerable time and generate a large volume of data.

[88] Partial panoramas (i.e., image mosaics less than 360° in size) will be the most common use of Pancam. These can be monochromatic or in many colors, and they typically will be targeted on the basis of images from the lower-resolution Navcams. We will acquire some images with full multispectral coverage, using all of the instrument's geology filters. This will be done when testing of a specific hypothesis requires determination of spectrophotometric properties across the full spectral range of the camera. The spatial coverage of full multispectral imaging will be restricted significantly by time and data volume limitations, so such images will need to be targeted carefully on the basis of previous Navcam or other Pancam imaging.

[89] Imaging of the Martian sky will be conducted on a regular basis to monitor atmospheric conditions. The Sun will be imaged directly through both solar filters to determine wavelength-dependent optical depth, and the sky will be imaged through the geology filters over a range of angular distance from the Sun to determine aerosol scattering properties.

[90] Pancam will be used to conduct several kinds of coordinated observations with other instruments. For example, we commonly will conduct both full multispectral Pancam imaging and Mini-TES rastering on candidate targets for in situ investigation in order to obtain morphologic, textural, and compositional information before making the decision to drive the rover.

[91] We also will use Pancam in tandem with the Microscopic Imager (MI), because engineering considerations made it impossible to package a filter wheel with the MI [*Herkenhoff et al.*, 2003]. We plan to acquire at least three-color Pancam images of every MI target. Software currently in development will allow us to register the lower-resolution Pancam color information with the higher-resolution textural information that the MI provides.

[92] Pancam will also be important for supporting the magnetic properties experiment [*Madsen et al.*, 2003]. The Capture and Filter magnets at the base of the PMA will be imaged in color on a regular basis to monitor the gradual buildup of magnetic dust. These images will be used to assess when the depth of dust is great enough to commit to making Mössbauer and APXS measurements of the magnets. The Sweep magnet is mounted directly adjacent to the Pancam calibration target, so it will be imaged with no

additional impact on time or data volume every time the target is imaged. The RAT magnets are located within the RAT, and after a RAT operation the Instrument Deployment Device will be used to position the RAT so that the magnets can be imaged in color by Pancam.

[93] Some of the most important operational considerations associated with Pancam are related to the large volume of data that the instrument can generate. By practical necessity, most Pancam data may end up being transmitted to Earth by UHF relay through the Mars Odyssey or Mars Global Surveyor (MGS) spacecraft. The latency associated with these links is substantial: up to 5 hours for Odyssey, and up to 2 days for MGS. Therefore most Pancam images will probably be used for strategic rather than tactical science planning, though judicious management of direct-to-Earth X-band downlink resources may allow an important subset of Pancam images (including 64 × 64 pixel "thumbnail" versions of all Pancam images acquired on each sol) to be downlinked more quickly [*Squyres et al.*, 2003]. Very careful selection of compression and downsampling parameters will also be essential to maximizing the science return from Pancam.

5.2. Commanding and Sequencing

[94] A single workhorse 47 parameter CAPTURE_IMAGE command in each rover's flight software provides most of the functionality required for Pancam imaging on Mars. This command automatically powers the cameras on and off, moves the PMA to a user-specified pointing position, actuates the filter wheel to the desired position, and establishes a number of other imaging parameters related to manual or automatic exposure time, exposure time scaling, compression level, downlink priority, etc. Multiple CAPTURE_IMAGE commands can be strung together to generate images at multiple pointings required for Pancam panoramas.

[95] Many more details of MER camera commanding, command buffering, and sequencing are described by *Maki et al.* [2003] and *Squyres et al.* [2003]. Of most relevance to Pancam is the capability to specify a set of relative exposure times among the Pancam filters (exposure tables), so that, for example, autoexposure mode can be used to image a scene through one filter, then simple relative filter-to-filter scaling from the exposure tables can be used to acquire much faster manual exposure images through the other filters. The exposure tables can be redefined and reuploaded on Mars, but by default they are generated based on the known responsivity variations among the Pancam filters, and an assumed average spectral radiance of typical bright Mars soil.

5.3. Onboard Image Postprocessing

[96] The rovers' flight software provides a substantial amount of capability for doing onboard image processing prior to downlink, with the primary goal to increase the compressibility of images and thus to maximize the amount of data that can be sent back to Earth during each downlink session. The image processing services offered by the rover CPU include bad pixel correction, flatfield correction, frame transfer smear correction, image downsampling, image subframing, pixel summing, 12 to 8 bit scaling via lookup tables, and image compression.

[97] Details of the implementation of all of these image processing capabilities are provided by *Maki et al.* [2003]. However, frame transfer smear correction deserves special notice because of its importance and implications for Pancam imaging. As discussed above, there are analytic or empirical ways to remove frame transfer smear signal from Pancam images. The main advantage of the a posteriori analytic approach of modeling the effect is that no additional image acquisition time or processing time are required on Mars. However, the uncorrected images to be downlinked are likely to be less compressible than corrected images, and substantial additional postprocessing time is required in the ground calibration pipeline. The main advantage of the in situ empirical approach of subtracting a zero-exposure image is that the removal of the bias, storage region dark current, and frame transfer ramp components should produce a much more compressible image for downlink than images that have not been corrected. The price for this increased downlink efficiency, though, is a doubling of the time required to acquire images, plus additional overhead for onboard CPU processing. It is anticipated that the tradeoffs will be made so that sometimes onboard frame transfer smear removal is more advantageous, while sometimes postprocessing analytic removal may be more advantageous. Each situation will need to be considered on a case by case basis.

[98] Rapid lossless onboard compression of MER camera images can be performed using a routine called LOCO, which is based on the same kind of segmented discrete cosine transform method as the JPEG compressor. High-quality lossy compression can be performed using a routine called ICER, which is a wavelet-based progressive compression routine that has been shown in tests by the MER science team to retain excellent image quality even at relatively high compression rates below 1 bit per pixel (compression ratios exceeding 12:1 for MER images). Additional information and details on both the LOCO and ICER compression routines for MER can be found in the work of *Maki et al.* [2003].

5.4. Inflight Calibration

[99] Monitoring of the stability of the Pancam spatial response pattern (flatfield) will be performed during flight by occasional imaging of the Martian sky (which, if the azimuth and elevation relative to the Sun are chosen properly, should be acceptably flat over the field of view of Pancam [e.g., *Tomasko et al.*, 1999]). If variations are detected because of, for example, dust particles on the Pancam external sapphire window, then these flatfields may be used in place of the preflight ground flatfields in the Pancam calibration pipeline.

[100] Monitoring of the Pancam radiometric calibration stability will be performed on Mars by frequent imaging of the Pancam calibration target under repeatable illumination conditions, and by occasional downlinking of reference pixel and dark current images. Imaging of the Sun and potentially certain bright standard stars at night may also provide additional information on calibration stability.

[101] A baseline for Mars surface calibration performance of Pancam (and other MER instruments) will be established during a "calibration campaign" to be performed shortly after each rover's landing. Observations planned for this

campaign include baseline calibration target imaging, dark current and reference pixel images, sky flatfields, and reassessment of PMA pointing by imaging surveyed fiducial marks on the rover deck and lander. In addition to validating (or not) the preflight calibration coefficients and overall camera and PMA performance, these baseline measurements will be used to monitor the potential build up of dust over time on either the camera optics or the surfaces of the Pancam calibration targets or magnetic properties experiment magnets.

5.5. Data Processing and Products

[102] MER rover imaging telemetry will be depacketized and converted into raw Experiment Data Records (EDRs) that conform to the Planetary Data System (PDS) image format. Standard Pancam data processing steps will vary depending on the level of processing performed on the rover prior to downlink. Typical steps include bias and dark current subtraction, frame transfer smear correction, flatfielding, and conversion to radiometric units (either radiance ($W/m^2/nm/sr$) or I/F, where I is the measured radiance and πF is the incident irradiance of sunlight at the top of the Martian atmosphere). The primary Pancam standard data product will be Reduced Data Record (RDR) image files in PDS format and calibrated to radiance. These EDRs and RDRs will be archived with the PDS and released to the community on the schedule outlined in *Arvidson* [2003]. In addition, EDRs will be converted to JPEGs and streamed onto the World Wide Web in real time as the downlink is received. Pancam image processing will be performed using routines written in the Interactive Data Language (IDL) programming environment. Details of the calibration algorithms and calibration data files are described separately [*Bell et al.*, 2003a, 2003b]; the in-flight application of the calibration pipeline will be the subject of a subsequent paper dedicated to this topic.

[103] Other special data products that will be generated from Pancam images include quick-look mosaics in simple cylindrical and vertical projections, anaglyphs and other stereogrammetric products like digital terrain models [*Kirk et al.*, 1999], fused mosaics of Pancam/Navcam and Pancam/Hazcam data sets, ''colorized'' MI or Navcam images for regions with coregistered Pancam and MI or Navcam data [e.g., *Herkenhoff et al.*, 2003], and false color maps of spectral parameters like band ratios, band depth maps, or spectral mixture model results [e.g., *Adams et al.*, 1986; *McSween et al.*, 1999; *Bell et al.*, 2000, 2002].

6. Summary

[104] This paper has provided an introduction and overview of the goals, design, specifications, and planned utilization of the Mars Exploration Rover mission Pancam instrument investigation. Pancam will obtain high resolution, stereoscopic, multispectral images from 400 to 1000 nm that are designed to provide data to test hypotheses regarding the geomorphology, composition, atmospheric properties, and evolutionary history of the two MER landing sites in early 2004. Pancam will also provide Sun-sensing and other data critical to the safe and efficient navigation of the rovers on Mars. Substantial additional detail on the testing, calibration, and performance of Pancam can be found in ancillary publications by *Bell et al.* [2003a, 2003b] available by request from the first author or via links to the Pancam investigation from the Athena public web site: http://athena.cornell.edu. Important additional aspects of the Pancam investigation, many of which are common to all the MER cameras, can also be found in the complementary publications regarding the MER engineering cameras and onboard image processing capabilities [*Maki et al.*, 2003], the MI [*Herkenhoff et al.*, 2003], the Magnetic Properties experiment [*Madsen et al.*, 2003], and the overall operational strategy of the entire MER Athena payload suite [*Squyres et al.*, 2003].

[105] **Acknowledgments.** Many people besides the formal authors of this paper have contributed substantially to the design, fabrication, and testing of the MER Pancam investigation. These people include members of the JPL and vendor MER camera fabrication and QA teams (Dave Thiessen, Darryl Day, Ali Pourangi, Pete Kobzef, Greg Lievense, Alejandro Soto, Nancy Cowarden, Calvin Grandy, Len Wayne, Mary White, Bobbie Woo), members of the JPL MER Project management staff (Pete Thiesinger, Barry Goldstein, Richard Cook, John Callas, Joy Crisp, and other members of the JPL MER Science Office staff), members of the JPL MER ATLO team (Matt Wallace, Raul Romero, Art Thompson, Leo Bister, and the rest of the highly capable ATLO staff), members of the Pancam calibration target design, fabrication, and test team (Dan Britt, Larry Stark, Jon Lomberg, Lou Friedman, Tyler Nordgren, Bill Nye, Patrick Pinet, Pascal Depoix, Yves Daydou), members of the Athena Instrument Calibration Peer Review Board (Steve Baloga, Paul Lucey, Ken Klaasen, and Bob West), and team members, associates, and students from the Athena Science Team who provided many long hours of support and Frappucinos during Pancam subsystem and system-level calibration, testing, and data analysis (Lisa Gaddis, Jim Torson, Jeff Johnson, Larry Soderblom, Doug Ming, Bill Farrand, Mike Wolff, Scott McClennan, Ed Guinness, Frank Seelos, Cathy Weitz, John Grant, Morten Madsen, Walter Goetz, Roger Tanner, Zoe Learner, Jason Soderblom, Yong Shin, Salman Arif, Stephanie Gil). To these and the many other unsung colleagues that have helped get Pancam and the MER rovers from blueprints to the launch pad and then on their way to Mars, we extend our deep and sincere gratitude.

References

Adams, J. B., Visible and near-infrared diffuse reflectance spectra of pyroxenes as applied to remote sensing of solid objects in the solar system, *J. Geophys. Res.*, *79*, 4829–4836, 1974.

Adams, J. B., M. O. Smith, and P. E. Johnson, Spectral mixture modeling: A new analysis of rock and soil types at the Viking Lander 1 site, *J. Geophys. Res.*, *91*, 8098–8112, 1986.

Arvidson, R., MER archive generation, validation, and transfer plan, *Rep. MER 420-1-200/JPL D-19658*, Jet Propul. Lab., Pasadena, Calif., 2003.

Arvidson, R. E., J. L. Gooding, and H. J. Moore, The Martian surface as imaged, sampled, and analyzed by Viking Landers, *Rev. Geophys.*, *27*, 39–60, 1989.

Baker, L. R., R. M. Scott, K. J. Ando, D. S. Lowe, and H. R. Luxenberg, Electro-optical remote sensors with related optical sensors, in *Manual of Remote Sensing*, chap. 7, pp. 325–366, Am. Soc. Photogramm., Falls Church, Va., 1975.

Bell, J. F., III, Iron, sulfate, carbonate, and hydrated minerals on Mars, in *Mineral Spectroscopy*: *A Tribute to Roger G. Burns*, edited by M. D. Dyar, C. McCammon, and M. W. Schaefer, *Spec. Publ. Geochem. Soc.*, *5*, 359–380, 1996.

Bell, J. F., III, T. B. McCord, and P. D. Owensby, Observational evidence of crystalline iron oxides on Mars, *J. Geophys. Res.*, *95*, 14,447–14,461, 1990.

Bell, J. F., III, et al., Mineralogic and compositional properties of Martian soil and dust: Results from Mars Pathfinder, *J. Geophys. Res.*, *105*, 1721–1755, 2000.

Bell, J. F., III, W. H. Farrand, J. R. Johnson, and R. V. Morris, Low abundance materials at the Mars Pathfinder landing site: An investigation using spectral mixture analysis and related techniques, *Icarus*, *158*, 56–71, 2002.

Bell, J. F., III, et al., Mars Exploration Rover (MER) project Pancam calibration plan, *Rep. JPL D-19696/MER-420-1-438*, 51 pp., Jet Propul. Lab., Pasadena, Calif., 2003a.

Bell, J. F., et al., Mars Exploration Rover (MER) project Pamcam calibration report, *Doc. D-19826/MER-420-6-700*, Jet Propul. Lab., Pasadena, Calif., 2003b.

Bishop, J. L., H. Fröschl, and R. L. Mancinelli, Alteration processes in volcanic soils and identification of exobiologically important weathering products on Mars using remote sensing, *J. Geophys. Res.*, *103*, 31,457–31,476, 1998.

Brown, D. I., Cassini imaging science subsystem analog-to-digital uneven bit weighting report for the wide and narrow angle camera, *Rep. 5.1.9-1*, Jet Propul. Lab., Pasadena, Calif., 1997.

Burns, R. G., Rates and mechanisms of chemical weathering of ferromagnesian silicate minerals on Mars, *Geochim. Cosmochim. Acta*, *57*, 4555–4574, 1993.

Carr, M. H., *The Surface of Mars*, 226 pp., Yale Univ. Press, New Haven, Conn., 1981.

Christensen, P. R., and H. J. Moore, The Martian surface layer, in *Mars*, edited by H. H. Kieffer et al., pp. 686–729, Univ. of Ariz. Press, Tucson, 1992.

Christensen, P. R., et al., Miniature Thermal Emission Spectrometer for the Mars Exploration Rovers, *J. Geophys. Res.*, *108*(E12), 8064, doi:10.1029/2003JE002117, in press, 2003.

Cloutis, E. A., M. J. Gaffey, T. L. Jackowski, and K. L. Reed, Calibrations of phase abundance, composition, and particle size distribution for olivine-orthopyroxene mixtures from reflectance spectra, *J. Geophys. Res.*, *91*, 11,641–11,653, 1986.

Cornell, R. M., and U. Schwertmann, *The Iron Oxides*, John Wiley, Hoboken, N. J., 1996.

Eisenman, A. R., C. C. Liebe, and R. Perez, Sun sensing on the Mars Exploration Rovers, *IEEE Aerosp. Conf. Proc.*, *5*, 2249–2262, 2002.

Golombek, M. P., The Mars Pathfinder mission, *J. Geophys. Res.*, *102*, 3953–3965, 1997.

Golombek, M. P., et al., Overview of the Mars Pathfinder mission: Launch through landing, surface operations, data sets, and science results, *J. Geophys. Res.*, *104*, 8523–8554, 1999.

Gooding, J. L., Chemical weathering on Mars, *Icarus*, *33*, 483–513, 1978.

Graff, T. G., R. V. Morris, and P. R. Christensen, Effects of palagonitic and basaltic dust coatings on visible, near-IR, thermal emission and Moessbauer spectra of rocks and minerals: Implications for mineralogical remote sensing of Mars, *Eos Trans. AGU*, *83*(47), Fall Meet. Suppl., abstract P72A-0486, 2002.

Guinness, E. A., R. E. Arvidson, M. A. Dale-Bannister, R. B. Singer, and E. A. Bruckenthal, On the spectral reflectance properties of materials exposed at the Viking landing sites, *J. Geophys. Res.*, *92*, E575–E587, 1987.

Guinness, E. A., R. E. Arvidson, I. H. D. Clark, and M. K. Shepard, Optical scattering properties of terrestrial varnished basalts compared with rocks and soils at the Viking Lander sites, *J. Geophys. Res.*, *102*, 28,687–28,703, 1997.

Hapke, B., Bidirectional reflectance spectroscopy: 1. Theory, *J. Geophys. Res.*, *86*, 3039–3054, 1981.

Hapke, B., Bidirectional reflectance spectroscopy: 4. The extinction coefficient and the opposition effect, *Icarus*, *67*, 264–280, 1986.

He, X. D., K. E. Torrance, F. X. Sillion, and D. P. Greenberg, A comprehensive physical model for light reflection, *Comput. Graphics*, *25*, 175–186, 1991.

Herkenhoff, K., et al., Athena Microscopic Imager investigation, *J. Geophys. Res.*, *108*(E12), 8065, doi:10.1029/2003JE002076, 2003.

Holst, G. C., CCD arrays, cameras, and displays, 378 pp., SPIE Opt. Eng. Publ./JCD Publ., Bellingham, Wash., 1998.

Huck, F. O., G. R. Taylor, H. F. McCall, and W. R. Patterson, The Viking Mars lander camera, *Space Sci. Instrum.*, *1*, 189–241, 1975.

Huck, F. O., D. J. Jobson, S. K. Park, S. D. Wall, R. E. Arvidson, W. R. Patterson, and W. D. Benton, Spectrophotometric and color estimates of the Viking lander sites, *J. Geophys. Res.*, *82*, 4401–4411, 1977.

Izenberg, N. R., et al., In-flight calibration of the Near Earth Asteroid Rendezvous Mission's near infrared spectrometer, I. Initial calibrations, *Icarus*, *148*, 550–571, 2000.

Janesick, J. R., K. P. Klaasen, and T. Elliot, Charge-coupled device charge-collection efficiency and the photon transfer technique, *Opt. Eng.*, *26*, 972–980, 1987.

Johnson, J. R., et al., Preliminary results on photometric properties of materials at the Sagan Memorial Station, Mars, *J. Geophys. Res.*, *104*, 8809–8830, 1999.

Johnson, J. R., W. M. Grundy, and M. T. Lemmon, Dust deposition at the Mars Pathfinder landing site: Observations and modeling of the visible/near-infrared spectra, *Icarus*, *163*, 330–346, 2003.

Kirk, R. L., et al., Digital photogrammetric analysis of the IMP camera images: Mapping the Mars Pathfinder landing site in three dimensions, *J. Geophys. Res.*, *104*, 8869–8887, 1999.

Klingelhöfer, G., et al., Athena MIMOS II Mössbauer Spectrometer investigation, *J. Geophys. Res.*, *108*(E12), 8067, doi:10.1029/2003JE002138, in press, 2003.

Madsen, M., et al., Magnetic Properties Experiments on the Mars Exploration Rover Mission, *J. Geophys. Res.*, *108*(E12), 8069, doi:10.1029/2002JE002029, in press, 2003.

Maki, J. N., J. J. Lorre, P. H. Smith, R. D. Brandt, and D. J. Steinwand, The color of Mars: Spectrophotometric measurements at the Pathfinder landing site, *J. Geophys. Res.*, *104*, 8781–8794, 1999.

Maki, J. N., et al., Mars Exploration Rover engineering cameras, *J. Geophys. Res.*, *108*(E12), 8071, doi:10.1029/2003JE002077, in press, 2003.

Markiewicz, W. J., R. M. Sablotny, H. U. Keller, N. Thomas, D. Titov, and P. H. Smith, Optical properties of the Martian aerosols as derived from Imager for Mars Pathfinder midday sky brightness data, *J. Geophys. Res.*, *104*, 9009–9018, 1999.

McSween, H. Y., Jr., et al., Chemical, multispectral, and textural constraints on the composition and origin of rocks at the Mars Pathfinder landing site, *J. Geophys. Res.*, *104*, 8679–8716, 1999.

Moore, H. J., D. B. Bickler, J. A. Crisp, H. J. Eisen, J. A. Gensler, A. F. C. Haldemann, J. R. Matijevic, L. K. Reid, and F. Pavlics, Soil-like deposits observed by Sojourner, the Pathfinder rover, *J. Geophys. Res.*, *104*, 8729–8746, 1999.

Morris, R. V., and T. G. Graff, Athena instrument validation and data library development for the Mars Exploration Rover (MER) mission, *Eos Trans. AGU*, *83*(47), Fall Meet. Suppl., abstract P21C-03, 2002.

Morris, R. V., H. V. Lauer Jr., C. A. Lawson, E. K. Gibson Jr., G. A. Nace, and C. Stewart, Spectral and other physiochemical properties of submicron powders of hematite (α-Fe_2O_3), maghemite (γ-Fe_2O_3), magnetite (Fe_3O_4), goethite (α-FeOOH), and lepidocroicite (γ-FeOOH), *J. Geophys. Res.*, *90*, 3126–3144, 1985.

Morris, R. V., D. C. Golden, J. F. Bell III, H. V. Lauer Jr., and J. B. Adams, Pigmenting agents in Martian soils: Inferences from spectral, Mossbauer, and magnetic properties of nanophase and other iron oxides in Hawaiian palagonitic soil PN-9, *Geochim. Cosmochim. Acta*, *57*, 4597–4609, 1993.

Morris, R. V., et al., Mineralogy, composition, and alteration of Mars Pathfinder rocks and soils: Evidence from multispectral, elemental, and magnetic data on terrestrial analogue, SNC meteorite, and Pathfinder samples, *J. Geophys. Res.*, *105*, 1757–1817, 2000.

Mutch, T. A., R. E. Arvidson, J. W. Head III, K. L. Jones, and R. S. Saunders, *The Geology of Mars*, 400 pp., Princeton Univ. Press, Princeton, N. J., 1976.

Patterson, W. R., III, F. O. Huck, S. D. Wall, and M. R. Wolf, Calibration and performance of the Viking lander cameras, *J. Geophys. Res.*, *82*, 4391–4400, 1977.

Pinet, P., F. Boubault, Y. Daydou, and S. Chevrel, Implementation of a laboratory wide field spectral imaging facility, *Eur. Geophys. Soc. Spring Meet*, abstract aac6327, 2000.

Pollack, J. B., D. S. Colburn, F. M. Flaser, R. Kahn, C. E. Carlston, and D. Pidek, Properties and effects of dust particles suspended in the Martian atmosphere, *J. Geophys. Res.*, *84*, 2929–2945, 1979.

Pollack, J. B., M. E. Ockert-Bell, and M. K. Shepard, Viking Lander image analysis of Martian atmospheric dust, *J. Geophys. Res.*, *100*, 5235–5250, 1995.

Reid, R. J., et al., Imager for Mars Pathfinder (IMP) image calibration, *J. Geophys. Res.*, *104*, 8907–8926, 1999.

Roush, T. L., D. L. Blaney, and R. B. Singer, The surface composition of Mars as inferred from spectroscopic observations, in *Remote Geochemical Analysis*: *Elemental and Mineralogical Composition*, edited by C. Pieters and P. Englert, pp. 367–393, Cambridge Univ. Press., New York, 1993.

Rover Team, The Pathfinder Microrover, *J. Geophys. Res.*, *102*, 3989–4001, 1997.

Sharp, R. P., and M. C. Malin, Surface geology from Viking landers on Mars: A second look, *Geol. Soc. Am. Bull.*, *95*, 1398–1412, 1984.

Shepard, M. K., The Bloomsburg Univ. Goniometer (B.U.G.) laboratory: An integrated laboratory for measuring bidirectional reflectance functions, *Lunar Planet. Sci.*, *XXXII*, abstract 1015, 2001.

Shepard, M. K., and R. E. Arvidson, The opposition surge and photopolarimetry of fresh and coated basalts, *Icarus*, *141*, 172–178, 1999.

Sherman, D. M., R. G. Burns, and V. M. Burns, Spectral characteristics of the iron oxides with application to the Martian bright region mineralogy, *J. Geophys. Res.*, *87*, 10,169–10,180, 1982.

Singer, R. B., Spectral evidence for the mineralogy of high-albedo soils and dust on Mars, *J. Geophys. Res.*, *87*, 10,159–10,168, 1982.

Sitter, D. N., Jr., J. S. Goddard, and R. K. Ferell, Method for the measurement of the modulation transfer function of sampled image systems from bar-target patterns, *Appl. Opt.*, *34*, 751–757, 1995.

Smith, G. H., E. C. Hagerott, L. M. Scherr, K. E. Herkenhoff, and J. F. Bell III, Optical designs for the Mars '03 Rover cameras, in *Current Developments in Lens Design and Optical Engineering II*, edited by R. E. Fischer, R. B. Johnson, and W. J. Smith, *Proc. SPIE Int. Soc. Opt. Eng.*, *4441*, 118–131, 2001.

Smith, P. H., and M. Lemmon, Opacity of the Martian atmosphere measured by the Imager for Mars Pathfinder, *J. Geophys. Res.*, *104*, 8975–8986, 1999.

Smith, P. H., et al., The Imager for Mars Pathfinder experiment, *J. Geophys. Res.*, *102*, 4003–4025, 1997a.

Smith, P. H., et al., First results from the Pathfinder camera, *Science*, *278*, 1758–1765, 1997b.

Soderblom, L. A., The composition and mineralogy of the Martian surface from spectroscopic observations: 0.3–50 μm, in *Mars*, edited by H. Kieffer et al., pp. 557–593, Univ. of Ariz. Press, Tucson, 1992.

Squyres, S. W., et al., Athena Mars Rover science investigation, *J. Geophys. Res.*, *108*(E12), 8062, doi:10.1029/2003JE002121, in press, 2003.

Thomas, N., W. J. Markiewicz, R. M. Sablotny, M. W. Wuttke, H. U. Keller, J. R. Johnson, R. J. Reid, and P. H. Smith, The color of the Martian sky and its influence on the illumination of the Martian surface, *J. Geophys. Res.*, *104*, 8795–8808, 1999.

Tomasko, M. G., L. R. Doose, M. Lemmon, P. H. Smith, and E. Wegryn, Properties of dust in the Martian atmosphere from the Imager on Mars Pathfinder, *J. Geophys. Res.*, *104*, 8987–9008, 1999.

H. M. Arneson, J. F. Bell III, A. G. Hayes, M. J. Johnson, J. Joseph, J. N. Sohl-Dickstein, S. W. Squyres, and R. J. Sullivan, Department of Astronomy, Cornell University, 402 Space Science Building, Ithaca, NY 14853-6801, USA. (hma6@cornell.edu; jfb8@cornell.edu; agh4@cornell.edu; mjj8@cornell.edu; jj21@cornell.edu; jns9@cornell.edu; squyres@astrosun.tn.cornell.edu; sullivan@cuspif.tn.cornell.edu)

D. Brown, S. A. Collins, A. Dingizian, S. T. Elliot, E. C. Hagerott, J. N. Maki, L. Scherr, M. Schwochert, and M. Wadsworth, Jet Propulsion Laboratory, California Institute of Technology, 4800 Oak Grove Drive, Pasadena, CA 91109, USA. (dbrown@mail1.jpl.nasa.gov; stewart.a.collins@jpl.nasa.gov; arsham.dingizian@jpl.nasa.gov; stythe.t.elliot@jpl.nasa.gov; edward.c.hagerott@jpl.nasa.gov; justin.n.maki@jpl.nasa.gov; lawrence.m.scherr@jpl.nasa.gov; mark.a.schwochert@jpl.nasa.gov; mark.v.wadsworth@jpl.nasa.gov)

K. E. Herkenhoff and J. R. Johnson, Branch of Astrogeology, United States Geological Survey, 2255 North Gemini Drive, Flagstaff, AZ 86001-1698, USA. (kherkenhoff@usgs.gov; jrjohnson@usgs.gov)

K. Kinch, Institute for Physics and Astronomy, University of Aarhus, DK-8000 Aarhus, Denmark. (kjartan@ifa.au.dk)

M. T. Lemmon, Department of Atmospheric Science, Texas A&M University, College Station, TX 77843-4242, USA. (lemmon@physics.tamu.edu)

R. V. Morris, NASA Johnson Space Center, Mail Code SN3, Houston, TX 77058, USA. (richard.v.morris1@jsc.nasa.gov)

M. K. Shepard, Department of Geography and Geosciences, Bloomsburg University, 400 East Second Street, Bloomsburg, PA 17817, USA. (mshepard@bloomu.edu)

G. H. Smith, GHS Optics, Pasadena, CA 91101, USA. (raybender@att.net)

W. T. Sullivan, Department of Astronomy, University of Washington, Seattle, WA 98195, USA. (woody@astro.washington.edu)